Title

Silicate weathering along an uplifting basaltic range on the Nicoya Peninsula, Costa Rica

Author

Horton, Elizabeth

Publication Date

2024

UNIVERSITY OF CALIFORNIA

Santa Barbara

Silicate weathering along an uplifting basaltic range on the Nicoya Peninsula, Costa Rica

A Thesis submitted in partial satisfaction of the
requirements for the degree Master of Science
in Earth Science

by

Elizabeth Horton

Committee in charge:
Professor Gen Li, Chair
Professor Vamsi Ganti
Professor Francis Macdonald

December 2024

The thesis of Elizabeth Horton is approved.

Vamsi Ganti

Francis Macdonald

Gen Li, Committee Chair

September 2024

Silicate weathering along an uplifting basaltic range on the Nicoya Peninsula, Costa Rica

by

Elizabeth Horton

ACKNOWLEDGEMENTS

This project was primarily funded by NSF grant EAR-2046278 and supplemented by a UCSB Faculty Research Grant. Thank you to Gen Li, Francis Macdonald, and Vamsi Ganti for discussions on this project and for serving on a master's committee. Thank you to Emily Burt, Lena Capece, Laifeng Li, Nick Rollins and William Berelson for conducting lab work. Thank you to Brian Penserini and Marino Protti for assistance in fieldwork. Additional support and comments on this work were provided by Kristin Morell and Morgan Raven.

Most importantly, I want to thank my friends, family, and pets because I could not have pulled through this without them. This thesis is for Lindsay, Dozie, and Jonathan.

ABSTRACT

Silicate weathering along an uplifting basaltic range on the Nicoya Peninsula, Costa Rica

by

Elizabeth Horton

Tectonic uplift has been hypothesized to accelerate silicate weathering rates and have driven atmospheric CO_2 drawdown in the late Cenozoic, yet quantifying tectonic control on silicate weathering rates is complicated by other rate-controlling factors like climate and lithology. The Nicoya Peninsula, Costa Rica, provides a unique opportunity to assess how silicate weathering rates vary across a tenfold variation in uplift rates under near-constant climate and basaltic lithology. Here we report stream water chemistry and ^{87}Sr/^{86} Sr ratios from 12 catchments draining mountainous terrain on Nicoya. From stream water chemistry, we partitioned weathering solutes from silicates and carbonates and then estimated catchment-scale stream discharge and sediment flux by calibrating global empirical models against hydrological gauging data in neighboring catchments. Combining these data, we determined the catchments' total denudation and silicate weathering rates and find that weathering on Nicoya is 'kinetically-limited', or where silicate weathering rates no longer increase linearly with denudation rates. The deviation from linear behavior is related to the extent of low-relief geomorphic surfaces (known as the Cerro Azul surface) in catchments, which likely sets sediment residence time and weathering duration. Nicoya falls at the high end of a global trend between temperature and basaltic weathering rates, supporting the temperature dependence of basalt weathering. Sr isotopic data confirms low ^{87}Sr/^{86}Sr ratios from basalt weathering and suggest that the weathering of mafic lithologies in tropical margins would not increase Cenozoic seawater Sr ratios. This study enhances our understanding of silicate weathering in an uplifting tropical basaltic range, while also highlighting geomorphic controls on silicate weathering.

TABLE OF CONTENTS

1. INTRODUCTION

Silicate weathering represents a major long-term CO_2 sink, regulating atmospheric CO_2 levels and Earth's climate over geological timescales (Chamberlin, 1899; Walker & Hays, 1981; Berner et al., 1983; Hilton & West, 2020; Brantley et al., 2023). Silicate weathering occurs as CO_2 dissolves in water to form carbonic acid (H_2CO_3), which reacts with silicate minerals and converts them to dissolved ions (Meybeck, 1987; Sundquist & Visser Ackerman, 2014). Weathering products are then transported to the oceans, where they are buried as carbonate rocks over million-year timescales (Berner et al., 1983; Walker & Hays, 1981; Sundquist & Visser Ackerman, 2014).

A comprehensive understanding of how tectonic uplift affects silicate weathering rates is critical for assessing the long-term evolution of Earth's climate state. Previous studies hypothesize that tectonic uplift enhanced erosion, accelerated silicate weathering, and drove global cooling in the late Cenozoic based on the synchrony of mountain growth and global cooling in the geological past (Raymo et al., 1989; Raymo & Ruddiman, 1992). For example, seawater $^{87}Sr/^{86}Sr$ ratios elevated in the late Cenozoic, indicating enhanced input of more radiogenic Sr flux (e.g., from weathering of silicate continents or other radiogenic lithologies) (Edmond, 1992; Raymo & Ruddiman, 1992; Li & Elderfield, 2013). In this paradigm, silicate weathering rates are expected to continually increase with denudation rates. Other studies suggest that mountain uplift enhanced global weatherability but not total weathering flux, such that global weathering rates remained less changed under tectonic uplift (Caves Rugenstein et al., 2019; Macdonald et al., 2019; Martin et al., 2023). Studies of modern-day weathering patterns in river catchments show that silicate weathering rates transit from the 'supply-limited' to 'kinetically-limited' weathering regime as denudation rates increase. The supply-limited relationship occurs at low denudation rates (< ~100 t/km^2/yr) where congruent weathering occurs (West et al., 2005; Gabet & Mudd, 2009; West, 2012; Bufe et al., 2024) and silicate weathering rates increase linearly with denudation rates. The kinetically-limited relationship occurs at high denudation rates (> ~100 t/km^2/yr) (West et al., 2005; Gabet & Mudd, 2009; West, 2012; Bufe et al., 2024), where silicate weathering rates no longer increase linearly with denudation rates and fall below the supply-limited boundary. It has been proposed that under high denudation rates, silicate weathering rates vary as a function of factors that affect reaction kinetics (e.g., temperature and runoff) (West et al., 2005; West, 2012). However, covariations between denudation rates, environmental conditions (e.g., lithology and associated weatherability), and kinetic factors in existing global datasets (West et al., 2005; West, 2012; Bufe et al., 2022, 2024) obscure our understanding of how uplift affects silicate weathering rates.

The Nicoya Peninsula, Costa Rica provides a unique setting for assessing the influence of tectonic uplift on silicate weathering. On the peninsula, a tenfold variation in uplift rates (LaFromboise, 2012) occurs under a near-uniform tropical climate and predominantly basaltic lithology. In addition, low-relief geomorphic surfaces known as the Cerro Azul surface form a mountainous backbone on the Nicoya Peninsula (Hare & Gardner, 1985). These surfaces allow us to assess how landscape configuration impacts silicate weathering rates (Jacobson et al., 2003; Jacobson & Blum, 2003; Porder et al., 2015; Torres et al., 2015). The prevalent basaltic bedrock and the tropical climate also offer an opportunity to constrain basalt weathering under warm surface temperatures, as previous studies have observed a global temperature dependence of basalt weathering (Dessert et al., 2003; Li et al., 2016; Chen et al., 2020) which has important implications for how the weathering of mafic terrain in the tropics affects Earth's climate (Macdonald et al., 2019; Park et al., 2020).

Using the unique field setting of the Nicoya Peninsula, we investigate the relationships between uplift, denudation, and silicate weathering along an uplifting basaltic range in the tropics. We measure the water chemistry in catchments that span the uplift gradient and derive silicate weathering and denudation fluxes using geochemical analyses, empirical modeling, and end-member mixing calculations. Based on our results, we determine how silicate weathering rates vary in response to the uplift gradient on Nicoya and discuss the implications of how tectonic uplift, geomorphology, and climatic conditions affect silicate weathering.

2. GEOLOGIC AND CLIMATIC SETTING

The Nicoya Peninsula sits along the Costa Rican portion of the Middle America Trench (MAT), where the Cocos Plate subducts northeastward beneath the Caribbean Plate at a rate of ~77 mm/yr (Fig. 1a) (DeMets et al., 2010). Pleistocene to Holocene marine terraces record average uplift rates that vary between 0.15-1.5 mm/yr along the peninsula's Pacific coastline (Figs. 1d & e) (LaFromboise, 2012). These uplift rates were determined by correlations between soil profiles of terraces and then comparison of linked terraces to a sea level curve, radiocarbon ages, and Optically Stimulated Luminescence (OSL) ages of terrace deposits (LaFromboise, 2012). In the northwest, uplift rates range between 0.1-0.2 mm/yr and increase to 0.25-0.35 mm/yr towards the southeast before rapidly increasing to 1-2 mm/yr at the peninsula's southern tip (Figs. 1d & e) (LaFromboise, 2012).

Elevations in the study area range from 0-1020 m, but a large portion of the study area is characterized by mountainous terrain with mean elevations ranging between 100-600 m (Figs. 1b & c). This mountainous terrain is largely comprised of a set of correlative geomorphic surfaces together known as the Cerro Azul surface (Fig. 1b) (Hare & Gardner, 1985).These surfaces were originally identified and mapped in the field by Hare & Gardner (1985) and are hypothesized to be paleo-abrasion surfaces (i.e., relict landscapes) that previously graded to sea level but were abandoned and incised in response to rock uplift. On top of the Cerro Azul surface, topography is subdued and deeply weathered, thick (5-10 m) soils occur (Hare & Gardner, 1985), indicative of the preservation of slower, relict erosion rates prior to incision and abandonment of the surface. The surface edges are flanked by steep (> 45°) continuous topographic scarps and fluvial knickpoints 100s of meters in elevation, which suggest a transition into more rapid erosion rates and landscape transience below the surface (Hare & Gardner, 1985).

The bedrock on the Nicoya Peninsula is dominated by basalt with lesser amounts of sedimentary rocks. In the study area, bedrock largely consists of Mesozoic igneous oceanic plateau assemblages that are partially overlain by Upper Cretaceous to Quaternary deep and shallow water sedimentary overlap sequences (Fig. 1d) (Baumgartner et al., 1984; Denyer et al., 2013a-f; Andjić et al., 2018, 2019). The dominant Mesozoic oceanic plateau lithology is the Manzanillo Terrane (Fig. 1d), which is mainly composed of Lower and Upper Cretaceous (~94-89 Ma) oceanic plateau basalts, with minimal intrusions of gabbro and dolerite (Andjić et al., 2018, 2019). Basaltic and intrusive rocks of the Manzanillo Terrane show evidence of oceanic hydrothermal alteration and include assemblages of calcite, zeolites, chlorite, and pumpellyite in veins (de Boer, 1979; Kuijpers, 1980). The Upper Cretaceous to lower Eocene overlap sequence overlies the Manzanillo Terrane (Fig. 1d) and contains siliciclastic, carbonate, and siliceous sedimentary rocks that transition between deep and shallow marine environments (Andjić et al., 2018). Lowest in the sequence are turbiditic sequences with interbeds of black shales, siliceous and calcareous shales, and mudstones (Andjić et al., 2018). These rocks are overlain by shallow water sandstones and conglomerates, deep water limestones, and more turbiditic sequences with local intercalations of siliceous limestones (Fig. 1d) (Andjić et al., 2018).

The Nicoya Peninsula occurs in Costa Rica's North Pacific climate zone and has a dry-to-sub-humid tropical climate with distinctly pronounced dry and wet seasons (Kappelle et al., 2016). The dry season occurs from December to April/mid-May and accounts for ~5% of annual rainfall, whereas the wet season occurs between mid-May to November and accounts for the remaining ~95% of annual rainfall (Kappelle et al., 2016). In the study area, mean annual rainfall rates derived from Tropical Rainfall Measurement Mission (TRMM) data (Bookhagen & Burbank, 2010) fluctuate less than 2-fold between about 1800-3000 mm/yr (Figs. 1f & g). Mean annual rainfall rates in sampled catchments range between 2101-3376 mm/yr and at most, vary by ~10% from mean annual rainfall rates in the study area (Fig. 1g). Temperatures on the Nicoya Peninsula are uniform intra-annually. In our study area, mean monthly temperatures (from the 1948-2024 National Centers for Environmental Prediction/National Center for Atmospheric Research or NCEP/NCAR dataset) (Kalnay et al., 1996) range between approximately 24.5-26.1 °C, with a mean annual temperature of 25 °C. Vegetation in the field area is mainly tropical dry forest and cattle pasture (Kappelle et al., 2016); however, our sampled catchments occur within relatively undisturbed, forested areas.

3. MATERIALS AND METHODS

To trace weathering solutes on Nicoya, we collected stream water samples from 12 catchments across the uplift gradient in the region and analyzed the water's chemical composition (cations, anions, dissolved inorganic carbon (DIC), and $^{87}Sr/^{86}Sr$ ratios). To determine total denudation rates, we employed empirical models that predict water and sediment fluxes for global catchments (Syvitski et al., 2003) and calibrated models against hydrological gauging data from neighboring catchments (National Climatic Data Center, NESDIS, NOAA, U.S. Department of Commerce, 2018). To characterize Nicoya's geomorphic setting, we computed relief and slope angles and mapped the Cerro Azul surface in the region from Digital Elevation Models (DEMs) (Insituto Geografico Nacional Costa Rica, 2019).

3.1. Field sampling

We collected stream water samples from 12 catchments along the uplift gradient on Nicoya in January 2022 (Figs. 1b, d & f; Table 1). The sampled catchments vary between small, mountainous, forested catchments to larger river valleys with occasional pasture and moderate floodplain development. Sampling sites were carefully selected to avoid anthropogenic disturbances. At sampling sites, we measured water temperatures using a thermometer and water pH using pH test strips, and collected one cation sample, one anion sample and one DIC sample. Stream water was collected in 50 mL plastic syringes and filtered through 0.22-µm pore-sized nylon syringe filters. Filtrates were used to clean the sampling containers before sample collection and were then collected in 60 mL Milli-Q-washed polypropylene bottles for anion analysis, in 60 mL acid-washed polypropylene bottles for cation analysis, and in 12 mL Labco exetainers for DIC analysis. Cation samples were acidified with 16 N high-purity nitric acid (HNO_3) to pH ~ 2.

3.2. Water chemistry measurements

Back in the laboratory, we measured total dissolved solids (TDS) and $^{87}Sr/^{86}Sr$ ratios of the water samples. Cation (K^+, Na^+, Ca^{2+}, Mg^{2+}) and dissolved Si concentrations were measured using an Inductively Coupled Plasma-Optical Emission Spectrometer (ICP-OES, iCAP-6300, Thermo Fisher Scientific) at Nanjing University (Li et al., 2024), with reported analytical uncertainties within ± 5% (2σ). Anion (Cl^- and SO_4^{2-}) concentrations were measured at the University of California Santa Barbara via ion chromatography on a Metrosep A Supp 5-100/4.0 column (Metrohm 930 Compact IC Flex) with a 0.32 M/0.1 M sodium carbonate/bicarbonate eluent. Reported analytical uncertainties were within ± 5% (2σ). DIC concentrations were measured at the University of Southern California using an Apollo DIC analyzer, with analytical uncertainties within ± 0.5% (2σ). $^{87}Sr/^{86}Sr$ ratios were measured using a Multicollecter-Inductively Coupled Plasma Mass Spectrometer (MC-ICP-MS, Neptune Plus) at Nanjing University, with analytical uncertainties reported at two standard deviations. The long-term mean $^{87}Sr/^{86}Sr$ of Reference Material NBS 987 was 0.710265 ± 0.00001 (mean ± 2σ, n = 15) and the measured $^{87}Sr/^{86}Sr$ values for the standard seawater IAPSO were 0.709111 ± 0.000024 and 0.709143 ± 0.000022, consistent with the recommended value (Liu et al., 2012; Li et al., 2024).

3.3. Digital topographic analysis and Cerro Azul surface mapping

To characterize the geomorphology of the peninsula, we analyzed a 5-m-resolution DEM which was reconstructed from 10-m topographic contours acquired from the Instituto Geográfico Nacional of Costa Rica (2019). We derived a hillshade map, slope, relief, 20-m contours, and a re-sampled 10-m DEM from the 5-m DEM in ArcGIS Pro. Slope was calculated over a 3 x 3 moving window, and relief was calculated as elevation range over a

1-km-radius moving window. We also delineated catchment boundaries for the 12 sampled catchments from the DEM and calculated the drainage area (A) for each catchment.

To constrain the extent of the Cerro Azul surface, we produced a new map of the surface with reference to the DEM-derived products and a low-resolution map by Hare & Gardner (1985). Specifically, we identified the Cerro Azul surface as high elevation areas with subdued topography bound by steep continuous topographic scarps. We mapped the edges of these high elevation areas as the boundaries of the Cerro Azul surface and supplemented our map with field observations of soil profiles and topography on top of mapped surfaces. We also computed mean local relief (in 250-m-radius windows) (Whipple et al., 2013) and slope across mapped Cerro Azul surfaces.

3.4. Stream discharge calculations

The sampled catchments lack field gauging data of stream discharge. In the absence of gauging data, we estimated annual stream discharge for sampled catchments by calibrating an empirical model (Syvitski et al., 2003) against gauged stream discharge from neighboring catchments in Costa Rica's North Pacific climate zone (National Climatic Data Center, NESDIS, NOAA, U.S. Department of Commerce, 2018) (Fig. S1), with reference to TRMM-derived precipitation data (Bookhagen & Burbank, 2010). The adopted empirical model is derived from a global dataset of 267 watersheds across Earth's major climate zones by fitting a power-law function between average annual stream discharge and watershed area:

$$\mathrm{Q} = \alpha_1 \mathrm{A}^{\alpha_2} \qquad \text{(Eq. 1)}$$

where Q is stream discharge (m^3/s), A is catchment area (km^2), and α_1 and α_2 are regression coefficients determined for each climate zone (Syvitski et al., 2003). We modeled stream discharge for the sampled catchments (Table 2) and gauged neighboring catchments using regression coefficients ($\alpha_1 = 0.53$, $\alpha_2 = 0.70$) fit to their corresponding climate zone, or the northern tropics (latitude of 0-30° N) (Tables S1 & S2).

To calibrate the empirical model, we derived decadal mean annual stream discharge of 5 gauged catchments adjacent to the Nicoya Peninsula in the North Pacific climate zone (Fig. S1) and compared the gauged stream discharge to those predicted from Eq. 1. The raw gauging dataset consisted of mean monthly discharges that were derived from daily discharges measured between 1973-1993 (National Climatic Data Center, NESDIS, NOAA, U.S. Department of Commerce, 2018). We excluded years with missing data and years with monthly records that did not span both the dry and wet season. The remaining records consisted of 4-11 years' worth of (a) complete datasets with 12 months of data, and (b) partially complete datasets with 8 months of data that captured the wet season and about 1.5 months of the dry season. For the 12-month datasets, we summed monthly discharge to derive an annual stream discharge. For the 8-month datasets, we calculated a mean monthly stream discharge and converted the monthly value to an annual discharge. We considered the 8-month datasets adequate substitutes for 12 months because their mean discharges were only at most 1.5 times higher. We then calculated the mean annual discharge over the 4-11 year-length records for all 5 gauged catchments and correlated the gauged stream discharge to modeled stream discharge (Eq. 1) to derive a calibration curve (Sec. 4.3.; Eq. 7).

As an additional constraint on the behavior of the empirical model in sampled versus gauged catchments, we calculated rainfall-equivalent stream discharges using TRMM data measured from 1998 to 2009 (Bookhagen & Burbank, 2010). We assume all rainfall converts to surface runoff without evapotranspiration and long-term groundwater storage losses (Erikson et al., 2024):

$$Q_t = PA \quad \text{(Eq. 2)}$$

where Q_t is rainfall-equivalent stream discharge (m^3/s) and P is TRMM-based mean annual rainfall (mm/yr) (Tables 2 & S2).

3.5. Sediment flux modeling

In the absence of measured physical erosion rates, we estimated the annual sediment flux in sampled catchments using an empirical model derived from the same global dataset of 267 rivers (Syvitski et al., 2003) which was used to derive the model for predicting stream discharge (Sec. 3.4). The sediment-flux model predicts annual sediment load (Q_{s0}, units kg/s) as a function of catchment area, catchment-scale relief, and mean annual temperature, yielding predictions within ± 20% of observed sediment loads (Syvitski et al., 2003):

$$Q_{s0} = \alpha_3 A^{\alpha_4} R^{\alpha_5} e^{kT_0} \quad \text{(Eq. 3)}$$

where R is catchment-scale relief (m, range of elevation within a catchment), T_0 is catchment-averaged temperature (°C), and α_3, α_4, α_5, and k are regression coefficients calibrated to Earth's major climate zones (Tables 2 & S1) (Syvitski et al., 2003).

To apply Eq. 3 to Nicoya, we used regression coefficients fit to the northern tropics (latitude 0-30° N): $k = -0.1$, $\alpha_3 = 0.31$, $\alpha_4 = 0.40$, and $\alpha_5 = 0.66$ (Table S1) (Syvitski et al., 2003). Catchment-scale relief was calculated from the 10-m DEM. Catchment-averaged mean annual temperatures were derived from NCEP/NCAR reanalysis temperature data provided by the NOAA Physical Sciences Laboratory in Boulder, Colorado, USA. The reanalysis data consists of 2.5° x 2.5° grids of 1000 millibar (mb) level mean monthly temperatures from 1948-2024 (Kalnay et al., 1996). Following the protocol established by Syvitski et al. (2003), we performed a series of corrections to provide more precise estimates of catchment-averaged temperatures which account for variations in latitudes and elevations (Syvitski et al., 2003). We first determined a lapse rate L(x) (°C/km), or the rate of temperature change with altitude as:

$$\mathrm{L(x)} = [\mathrm{a_0} \cos(\mathrm{a_1 x}) + \mathrm{a_2}]\{1 - \mathrm{a_3 e}[-(\mathrm{x/a_4})^2]\} \qquad \text{(Eq. 4)}$$

where x is the catchment-averaged latitude (°) calculated in ArcGIS Pro and a_0-a_4 are regression coefficients (a_0=2.609, =a_1 = 0.03, a_2 = 5.464, a_3 = 0.1252, a_4 = 33.77) (Tables 2 & S1) (Syvitski et al., 2003). We then used lapse rates to calculate catchment-averaged, mean annual temperatures (T_0, units °C) (Syvitski et al., 2003):

$$\mathrm{T_0} = \mathrm{T} + [\mathrm{L(x)H}] \qquad \text{(Eq. 5)}$$

where T is the mean annual temperature from the NCEP/NCAR reanalysis data and H is the catchment-averaged, mean elevation (km) calculated from the 10-m DEM (Table 2).

We used the resolved T_0, R, and A in Eq. 3 to predict annual sediment loads (Q_{s0}) in our sampled catchments based on the globally-calibrated model (Table 2). We further corrected Q_{s0} to account for the deviation of the prediction from the global model from the local gauging data (Sec. 3.4). We determined the concentration of sediment (C_s, units kg/m^3) in catchments between modeled sediment (Q_{s0}) and modeled stream discharge (Q) (Table 2):

$$\mathrm{C_s} = \mathrm{Q_{s0}/Q} \qquad \text{(Eq. 6)}$$

Sediment concentrations were then calibrated against corrected stream discharge (Sec. 4.3.). The resolved sediment fluxes were later combined with water chemistry data to estimate total denudation rates in sampled catchments (Sec. 5.1.2.).

4. RESULTS

4.1. Water chemistry

Stream water in sampled catchments is slightly alkaline (pH ~ 7-8) and has a mean temperature of ~26°C (Table 1). Under such pH and temperature conditions, DIC is dominated by HCO_3^- (Cole & Prairie, 2024), thus we assume that DIC concentrations can be approximated as HCO_3^- concentrations. The electric charges carried by the cations (TZ^+) are generally matched by those of the anions (TZ^-) with Normalized Inorganic Charge Balances (NICB, $||TZ^+| - |TZ^-|| / (|TZ^+| + |TZ^-|) \times 100\%$) within ~10% (Table 1).

Sampled catchments have TDS concentrations ranging from 2080-3071 mg/L (mean = 2486 ± 256 mg/L (1σ), Table 1). In decreasing order, the major cations with the highest concentrations are Ca^{2+} (656-1309 µM, mean = 862 ± 181 µM (1σ)), Mg^{2+} (429-722 µM, mean = 539 ± 82 µM (1σ)), Na^+ (272-521 µM, mean = 378 ± 62 µM (1σ)), and K^+ (7-15 µM, mean = 11 ± 3 µM (1σ)) (Table 1). Dissolved Si varies between 852-1139 µM (mean 1004 ± 74 µM (1σ)) (Table 1), constituting 15-21% of the TDS (by molar amount). Cl^-, SO_4^{2-}, and DIC have concentrations of 0-70 µM (mean = 48 ± 17 µM (1σ)), 20-35 µM (mean = 25 ± 4 µM (1σ)), and 2236-3634 µM (mean = 2851 ± 418 µM (1σ)), respectively (Table 1). Notably, except for one catchment (Sample 7) where Cl^- concentration is ~0 µM (Table 1), the concentrations of TDS, major cations and anions, dissolved Si, and DIC of all catchments all vary within a factor of around two (Figs. 2a-c). The dissolved $^{87}Sr/^{86}Sr$ ratios are relatively uniform between sampled catchments (0.7042-0.7066, mean = 0.705055 ± 0.000750 (1σ); Table 1; Fig. 2d), comparable to values of 0.7035-0.7053 reported from volcanic islands (Louvat, 1997) and slightly lower than the modal value (~0.710) of $^{87}Sr/^{86}Sr$ from a global dataset of 60 large rivers (Gaillardet et al., 1999).

4.2. Geomorphic characteristics of the Cerro Azul surface

We mapped nine patches of high elevation (~200-900 m) surfaces that cover a total area of 341 km^2 over 95 km along-strike the MAT between northwestern and southeastern Nicoya (Fig. 1a). Steep (25-50°), high relief (260-670 m), continuous topographic scarps (Figs. 3a & c) with bedrock streams (Fig. 3c) flank these surfaces. Topography on top of the surfaces is subdued relative to the topographic scarps (Figs. 3a-c). Across all nine surfaces, the mean slope and relief are $22° \pm 12°$ (1σ) and 125 ± 43 m (1σ), respectively. On top of several surfaces, we observe deeply-weathered, red soil profiles several meters thick, as well as occasional outcrops of bedrock and evidence of active bedrock erosion in streams (Figs. 3b & c). The distribution and characteristics of the surfaces we mapped are consistent with previous observations of the Cerro Azul surface in the region (Hare and Gardner, 1985).

4.3. Performance of stream discharge model

We establish a weighted linear relationship between the predicted annual stream discharge (Q from Eq. 1; Table 2) and the gauged annual stream discharge (Q_g; Table S2):

$$Q_c = 0.30Q - 0.38 \qquad \text{(Eq. 7)}$$

The fit in equation (7) is statistically significant, with $p < 0.05$, $R^2 = 0.93$, and uncertainty on the slope = 0.04 (Fig. 4a). Applying Eq. 7 to the sampled catchments, we obtain corrected annual stream discharge Q_c of 0.079-3.9 m^3/s, or 0.0025-0.12 km^3/yr (Table 2).

As an additional constraint on the model behavior, we compare the model-predicted, uncorrected stream discharge Q (Eq. 1) against TRMM-based stream discharge Q_t (Eq. 2) for both the 12 sampled catchments in Nicoya (Table 2) and the 5 North Pacific catchments selected for model calibration (Fig. S1; Table S2). We find a strong, consistent linear trend (R^2=0.97) between Q and Q_t for all catchments (Figs. 4b & c), suggesting a consistent model behavior between Nicoya and the North Pacific. Such consistency lends confidence to using gauged North Pacific catchments to calibrate stream discharge in Nicoya catchments.

The spatial variations in calibrated stream discharge (Table 2) and strong seasonality in rainfall on Nicoya allow an assessment of the relationship between solute concentrations and stream discharge. Riverine solute concentrations have been observed to vary with stream discharge over space and time, revealing a competition between chemical reactions (enhancing solute concentrations) and dilution processes (reducing solute concentrations) (Godsey et al., 2009; Maher & Chamberlain, 2014; Moon et al., 2014; Ibarra et al., 2016; Torres et al., 2017; Zhang et al., 2022). In our study, TDS concentrations from the January sampling season have minimal variations with TRMM-based estimates of mean January discharge (Fig. 5a). Across sampled catchments, mean January discharge varies by a factor of 27, whereas TDS concentrations only vary by a factor of 1.3, suggesting a near-chemostatic behavior (e.g., invariant solute concentrations against stream discharge) (Godsey et al., 2009; Torres et al., 2017). Notably, the mean monthly rainfall between Nicoya's dry (34 mm/month) and wet seasons (370 mm/month) varies by 11 times (Fig. 5b), much smaller than the factor of variation (~27) observed in the January discharge across sampled catchments. Thus, we consider that the spatial variation in January stream discharge captures intra-annual variation. As a result, the observed near-chemostatic behavior is representative for the full year (Godsey et al., 2009) This inference is used in Section 5.1 where we estimate silicate weathering rates.

4.4. Performance of sediment flux model

We calibrate annual sediment flux (Q_{sc}, units kg/s) using sediment concentrations (C_s, units kg/m^3) and corrected annual stream discharge (Q_c m^3/s):

$$Q_{sc} = C_s Q_c \quad \text{(Eq. 8)}$$

The annual calibrated sediment loads range from 0.089-2.4 kg/s or 2.8-76 kt/year across the sampled catchments (Table 2). Normalizing the sediment load by catchment area, we obtained sediment yields of 614-1671 t/km^2/yr, which translate into physical erosion rates of 0.20-0.56 mm/yr considering rock density (ρ = 3000 kg/m^3) for basalt, the dominant lithology in the region (Table 2). Physical erosion rates generally increase to the southeast along-strike of the MAT (Fig. S2), exhibiting a spatial pattern consistent with average uplift rates recorded by Pleistocene to Holocene marine terraces (0.15-1.5 mm/yr) (Fig. 1e) (LaFromboise, 2012). Assuming topographic steady state (Kirby & Whipple, 2012) and neglecting chemical denudation, we infer short-term uplift rates from sediment yields as 0.20-0.56 mm/yr, which are within the range recorded by Pleistocene to Holocene marine terraces (0.1-2 mm/yr) (LaFromboise, 2012). The deviation between these estimates is likely because sediment loads derived over shorter timescales may not adequately capture natural oscillations in sediment discharge from factors like climate or landscape transience (Wittmann et al., 2011).

5. DISCUSSION

In this section, we first quantify the silicate weathering and total denudation rates using our measurements and modeling results. We then discuss the weathering and denudation rates in the context of weathering regimes, the geomorphology of the Cerro Azul surface, and the implications for how tectonic uplift affects silicate weathering. Next, we compare our results to a global dataset of basalt weathering and discuss the influence of temperature on weathering rates of Nicoya basalts. Lastly, we discuss the implications of Sr isotopic data for chemical weathering histories in the late Cenozoic.

5.1. Silicate weathering and total denudation rate calculations

5.1.1. Unmixing of solute sources

We use a forward model (Meybeck, 1987; Moon et al., 2007; Bufe et al., 2022) to isolate dissolved solids from atmospheric and lithologic sources in sampled catchments. We exclude anthropogenic sources given the limited exposure to human activities in the study area. We assume that the primary atmospheric inputs are marine aerosols given Nicoya's coastal setting (Fig. 1a) (Meybeck, 1983; Kappelle et al., 2016). We consider carbonate and silicate rocks as primary lithologic sources as there are no evaporite outcrops in the region (Fig. 1d). This inference is supported by the observation that in a Na-normalized ratio space, all data from the sampled catchments fall on the mixing trends between silicates and carbonates (Figs. 6a & b). We note that although the study area is dominated by basaltic rocks with minor carbonate outcrops (e.g., overlap sequence rocks) (Fig. 1d), studies indicate that carbonate-enriched hydrothermal mineral assemblages and calcite veins (de Boer, 1979; Kuijpers, 1980) occur within basalts.

Below we introduce our workflow. We first correct for atmospheric inputs from marine aerosols in major ionic species (Ca^{2+}, Mg^{2+}, Na^{+}, K^{+}, HCO_3^{-}, $SO4^{2-}$, Cl^{-}) and dissolved Si using molar ratios for seawater (Table S3) (Byrne et al., 2024; Johnson, 2024). Cl^{-} serves as an index of atmospheric inputs to riverine solutes because in the absence of evaporite rocks, all Cl^{-} in stream water is expected to originate from atmospheric deposition (Gaillardet et al., 1999). We quantify atmospheric inputs to Na^{+} as:

$$[\mathrm{Na}]_{\mathrm{atmos}} = [\mathrm{Na/Cl}]_{\mathrm{atmos}} \text{ x } [\mathrm{Cl}]_{\mathrm{sample}} \qquad \text{(Eq. 9)}$$

where $[Na]_{atmos}$ is the atmospheric input to Na^{+} (Table S4), $[Na/Cl]_{atmos}$ is the molar ratio for seawater, and $[Cl]_{sample}$ is the Cl^{-} concentrations measured in water samples (Tables 1 & S4).

$[\mathrm{Na}]_{\mathrm{atmos}}$ serves as a normalization factor to determine the atmospheric contributions to other species (X):

$$[\mathrm{X}]_{\mathrm{atmos}} = [\mathrm{X/Na}]_{\mathrm{atmos}} \times [\mathrm{Na}]_{\mathrm{atmos}} \quad \text{(Eq. 10)}$$

where $[\mathrm{X}]_{\mathrm{atmos}}$ is the atmospheric input to X (Table S4) and $[\mathrm{X/Na}]_{\mathrm{atmos}}$ is the seawater molar ratio of a given ionic species. We then use atmospheric inputs to isolate contributions from the weathering of rocks $[\mathrm{X}]_{\mathrm{rock}}$ (Table S4):

$$[\mathrm{X}]_{\mathrm{rock}} = [\mathrm{X}]_{\mathrm{sample}} - [\mathrm{X}]_{\mathrm{atmos}} \quad \text{(Eq. 11)}$$

We next separate solutes from weathering of silicate versus carbonate rocks. With the absence of evaporites in the study area, we attribute the residual Na^+, K^+, and dissolved Si after correction for atmospheric inputs to source solely from silicate weathering (Meybeck, 1987; Moon et al., 2007; Bufe et al., 2022). Under the predominance of basalt in the field area, we attribute weathering solutes from silicates to approximately represent weathering of basalt. For Ca^{2+}, Mg^{2+}, and $\mathrm{HCO_3}^-$, we use the following equation to quantify contributions from silicate weathering:

$$[\mathrm{X}]_{\mathrm{sil}} = [\mathrm{X/Na}]_{\mathrm{sil}} \times [\mathrm{Na}]_{\mathrm{rock}} \quad \text{(Eq. 12)}$$

where $[\mathrm{X}]_{\mathrm{sil}}$ is the concentration from silicate weathering and $[\mathrm{X/Na}]_{\mathrm{sil}}$ is the Na-normalized molar ratio for silicate rocks. We adopt $[\mathrm{X/Na}]_{\mathrm{sil}}$ from an inversion modeling study of 60 large rivers (Gaillardet et al., 1999) (Figs. 6a & b; Table S3).

After resolving $[\mathrm{X}]_{\mathrm{sil}}$, we calculate the concentrations of X from carbonate weathering ($[\mathrm{X}]_{\mathrm{carb}}$) as:

$$[\mathrm{X}]_{\mathrm{carb}} = [\mathrm{X}]_{\mathrm{rock}} - [\mathrm{X}]_{\mathrm{sil}} \quad \text{(Eq. 13)}$$

Following Eqs. 9-13, we calculate the contributions to the dissolved chemical species from silicates and carbonates (Table S4). On average, carbonate weathering accounts for

86% of Ca^{2+}, 85% of Mg^{2+}, and 76% of HCO_3^- in our measured samples. In general, carbonate weathering is orders of magnitude faster than silicate weathering and can significantly contribute to total weathering fluxes even when present in minor amounts (Meybeck, 1987; Moon et al., 2014). On Nicoya, despite limited surficial exposure of carbonates (Fig. 1d), hydrothermal mineral assemblages and calcite veins (de Boer, 1979; Kuijpers, 1980) in basalts provide a source of carbonates for weathering. However, secondary carbonates, which may precipitate from soils and re-dissolve under wetter climates (Meng et al., 2015; Zamanian et al., 2016) are unlikely to contribute to carbonate solutes on Nicoya, as suggested by the lack of strong, positive relationships between Ca/Mg, Ca/Sr, and calibrated stream discharge (Fig. S3) (Li et al., 2023).

5.1.2. Silicate weathering and total denudation rate calculations

We use silicate cation denudation rates (SCDRs) to represent silicate weathering rates (West et al., 2005). SCDRs consist of the flux ($t/km^2/yr$) of cations derived from silicate weathering within a catchment and are calculated by integrating the total concentration of cations from silicate weathering ($[Cat]_{sil} = [Ca]_{sil} + [Mg]_{sil} + [Na]_{sil} + [K]_{sil}$, in mass units) over stream discharge (West et al., 2005). Given the near-chemostatic behavior of weathering processes in sampled catchments (Sec. 4.3.), we approximate SCDRs as the product of $[Cat]_{sil}$ and the calibrated annual stream discharge Q_c (Sec. 4.3.; Table 2) for each sampled catchment, normalized against catchment area:

$$\mathrm{SCDR} = [\mathrm{Cat}]_{\mathrm{sil}} \text{ x } \mathrm{Q_c} \qquad \text{(Eq. 14)}$$

Total denudation rates (TDR, $t/km^2/yr$) are the sum of the chemical denudation rates and physical erosion rates (West et al., 2005). Total chemical denudation rates (CDR) were calculated as the product of the total concentrations of major solutes from rock weathering

($[\mathrm{Conc}]_{\mathrm{rock}} = [\mathrm{Ca}]_{\mathrm{rock}} + [\mathrm{Mg}]_{\mathrm{rock}} + [\mathrm{Na}]_{\mathrm{rock}} + [\mathrm{K}]_{\mathrm{rock}} + [\mathrm{Si}]_{\mathrm{rock}} + [\mathrm{HCO_3}]_{\mathrm{rock}} + [\mathrm{SO_4}]_{\mathrm{rock}}$, in mass units) and calibrated annual stream discharge (Q_c), normalized against catchment area:

$$\mathrm{CDR} = [\mathrm{Conc}]_{\mathrm{rock}} \text{ x } \mathrm{Q_c} \qquad \text{(Eq. 15)}$$

Physical erosion rates (PER) are determined by normalizing the corrected sediment flux (Q_{sc}; Sec. 4.4.; Table 2) by catchment area (A):

$$\mathrm{PER} = \mathrm{Q_{sc}} / \mathrm{A} \qquad \text{(Eq. 16)}$$

TDR is then determined as:

$$\mathrm{TDR} = \mathrm{CDR} + \mathrm{PER} \qquad \text{(Eq. 17)}$$

In practice, we implement an iterative Monte Carlo random sampling approach to resolve SCDR and TDR and determine their uncertainties simultaneously. In each iteration, we resolve Eqs. 9-17 simultaneously and draw variables randomly from their distributions assigned by related uncertainties (uncertainty on [X]: analytical errors; uncertainty on Q_c: uncertainty on the slope of Eq. 7; uncertainty on Q_{sc}: 20% of predicted value (Syvtiski et al., 2003), uncertainty on $[X/Na]_{sil}$: Table S3 adopted from Gaillardet et al., (1999)). We run 1,000,000 iterations and report the mean ± 1σ of the result population for each catchment. The mean SCDR and TDR for each catchment range between 24-118 t/km^2/yr and 1872-5727 t/km^2/yr, respectively (Table 3).

5.2. Silicate weathering rate versus total denudation rate

5.2.1. Implications for weathering regime

We cast the resolved weathering and denudation rates into the TDR-SCDR space (West et al., 2005; Gabet & Mudd, 2009; West, 2012) and find that all sampled catchments and the mean of all sampled catchments (TDR: 4557 ± 975 t/km^2/yr; SCDR: 85 ± 24 t/km^2/yr; Table 3) fall within the kinetically-limited domain (Fig. 7a) (West et al., 2005;

Gabet & Mudd, 2009; West, 2012). Our data occurs in two groups. One group (consisting of 11 catchments) has TDRs (4057-5727 t/km^2/yr) comparable to some of the highest TDRs observed in alpine catchments (Fig. 7a) (West et al., 2005). SCDRs of those 11 catchments (67-118 t/km^2/yr) are higher than other catchments under similar TDRs (West et al., 2005; Bufe et al., 2024) and comparable to chemical weathering rates (19-326 t/km^2/yr) observed among other tropical basaltic settings (Louvat & Allègre, 1997; Louvat, 1997; Dessert et al., 2001, 2015; Moore et al., 2024), though we note that these fluxes are in part controlled by other factors such as tectonic setting and volcanic activity (Dessert et al., 2015). The other group consists of one catchment (Sample 5) that has a TDR of 1872 ± 943 t/km^2/yr and a SCDR of 24 ± 12 t/km^2/yr (Table 3), which are comparable to those of submontane and alpine catchments (Fig. 7a) (West et al., 2005) as well as tropical basaltic settings (Dessert et al., 2001; Moore et al., 2024).

On the Nicoya Peninsula, warm mean annual temperatures (27-30 °C) (Table 2), high mean annual rainfall (1800-3000 mm/yr) (Fig. 1g) and abundant highly-weatherable mafic rock (Fig. 1d) (Dupré et al., 2003) act in tandem to drive rapid silicate weathering. Despite these optimal environmental factors, silicate weathering remains kinetically-limited in the region, which we attribute to limits of weathering duration. Rapid rates of erosion ($> 10^2$ t/km^2/yr) (Gabet & Mudd, 2009) reduce the residence time of silicate minerals within the weathering zone, leading to incongruent weathering and a dependence on factors controlling the kinetics of weathering reactions (e.g., temperature and runoff) (West et al., 2005; West, 2012). Weathering limited by inadequate residence times is supported by the predominance of moderately-leached alfisols (Rust, 1983) in the study area (Ryan et al., 2024). In the next section, we explore how weathering behaviors link to the peninsula's geomorphology and the presence of the Cerro Azul surface in sampled catchments (Sec. 5.2.2).

5.2.2. Geomorphic controls on silicate weathering and implications for the uplift-weathering hypothesis

With the predominance of basalt (Fig. 1d), relatively invariable concentration-discharge relationships (Sec. 4.3.; Fig. 5a), and uniform temperatures across sampled catchments, we hypothesize that the extent of the Cerro Azul surface modulates weathering behavior. Low relief and inferred slow erosion rates on the Cerro Azul surface most likely permit silicate minerals longer residence times in the weathering zone, while steepened relief and landscape transience below the surface most likely reduce residence times. Several observations support this hypothesis. First, the 11 catchments with lower Cerro Azul surface coverage (0-49%) (Table 3) fall further from the supply-limited line ($\log_{10}$(residual)=2.4-2.6), whereas the catchment on top of the surface (Sample 5; 100% Cerro Azul coverage; Table 3) falls closer to the supply-limited line ($\log_{10}$(residual)=2.1) (Fig. 7b). In sample catchment 5, comparatively subdued topography on top of the Cerro Azul surface (Figs. 3a & b) likely slows catchment-wide erosion rates (Table 2; Fig. 7a) and promotes the development of meters-thick soils (Fig. 3b). These more erosively quiescent conditions afford silicate minerals longer weathering timespans before being eroded (West et al., 2005). However, in sample catchment 5, denudation rates still exceed the threshold of supply-limited weathering (>10^2 t/km^2/yr) (Gabet & Mudd, 2009), and host local zones of high topography (mean relief = 312 m; Table 2) where bedrock erosion likely occurs (Fig. 3b), preventing fully supply-limited weathering.

In contrast, high relief (260-670 m) and landscape transience in the topographic scarps below the Cerro Azul surface (Figs. 3a & c) accelerate erosion rates, which precludes thorough leaching of silicate cations into soils and drives silicate weathering further into the kinetically-limited regime. This is supported by a moderate positive correlation (R = 0.51) between catchment-averaged relief and distance from the supply-limited line (Fig. 7c). This transition is clearly revealed in a set of nested catchments (Samples 3, 4, and 5) (Fig. 3a). Below sample catchment 5, catchments 4 (mean relief=430 m; Table 3) and 3 (mean relief=414 m; Table 3) sample higher relief in the topographic scarp (Figs. 3a & c) and fall farther from the supply-limited boundary (Fig. 7c). Additionally, soil orders largely shift from strongly-leached utisols (Miller, 1983) on top of the surface to moderately-leached alfisols (Rust, 1983) below (Ryan et al., 2024), which supports the notion that the presence of the Cerro Azul surface drives variation in the weathering timescales of silicate minerals. This hypothesis is consistent with observations from a quartz diorite landscape in Puerto Rico, where weathering similarly transitions from supply-limited on top of low relief surfaces to kinetically-limited in transiently-adjusting knickzones below (Porder et al., 2015).

Multiple studies propose geomorphic controls of weathering processes (Jacobson et al., 2003; Jacobson & Blum, 2003; Porder et al., 2015; Torres et al., 2015), consistent with the findings from this study. Our results (Fig. 7) suggest that the geomorphic configuration of mountain ranges could influence the relationship between denudation rates and silicate weathering rates. In particular, the uplift of orogenic systems with low-relief plateaus (e.g., the Himalayan-Tibetan system) may have played a more nuanced role in enhancing silicate weathering (Raymo & Ruddiman, 1992). In Himalayan-Tibetan style orogenic belts where broad high elevation plateaus develop in the hinterland, silicate weathering rates may transit from kinetically-limited in steep mountain belts (Gabet et al., 2010) towards more supply-limited conditions on plateaus, similar to patterns observed for the Cerro Azul surface. This potential duality between weathering regimes suggests that uplift of broad plateaus in the hinterland could facilitate a more direct scaling between uplift, erosion, and silicate weathering, which then breaks down as erosion rates accelerate in steep mountain fronts.

5.3. Implications for basalt weathering and potential for carbon dioxide consumption

Our data allow us to constrain the weathering behavior of basalts on the Nicoya Peninsula and place them within a global context. We calculate the silicate-derived HCO_3^- fluxes (product of $[HCO_3^-]_{sil}$ and Q_c) as a proxy for basalt weathering rates (Table 3) (Dessert et al., 2003). At the warm mean annual temperatures (27-30°C) (Table 2) in sampled catchments, weathering-induced HCO_3^- fluxes range from (0.23-1.2) x 10^6 mol/km^2/yr with a mean ± 1σ of 0.93 ± 0.17 x 10^6 mol/km^2/yr (Table 3). We find that the average HCO_3^- flux (weighted by catchment area) falls onto a global trend between temperature and HCO_3^- flux of inactive basaltic fields (Fig. 8) (Li et al., 2016; Chen et al., 2020), although geomorphic modulation of weathering rates may partially interfere with weathering's relationship to temperature (Sec. 5.2.2.). Nonetheless, our data sit at the high end of Earth's surface temperature range, providing a key constraint on basalt weathering and supporting its temperature dependence under warm temperatures. If viewed as an additional proxy of CO_2 consumption rates (Li et al., 2016), weathering-induced fluxes of HCO_3^- from this study suggest that the sampled catchments consume an average of 0.93 x 10^6 mol/km^2/yr of CO_2, close to the upper bound of consumption rates observed in inactive tropical basaltic margins (0.1-1 x 10^6 mol/km^2/yr) (Dessert et al., 2003; Li et al., 2016). Our estimated CO_2 consumption rate from basalt weathering in Nicoya is lower than the CO_2 consumption potential (3.9-27 x 10^6 mol/km^2/yr) estimated in an experimental study of enhanced weathering for CO_2 removal using an andesitic soil chronosequence and basaltic andesites from Costa Rica, and the USGS basalt standard BHVO-1 (Ryan et al., 2024). This difference is likely because fine grain sizes from powdered materials in the experimental study provide greater reactive surface area than in natural erosional products (Ryan et al., 2024).

5.4. Implications for the Sr cycle

The measured ^{87}Sr/^{86}Sr ratios (0.7042-0.7066) in Nicoya stream water samples (Table 1) are consistent with ^{87}Sr/^{86}Sr ratios (0.705) of rivers draining < 2 Ga magmatic provinces (Gaillardet et al., 1999), reflecting the relatively young ages (~94-89 Ma) of the volcanic rocks of the Manzanillo Terrane (Andjić et al., 2019) (Fig. 6c). However, our samples deviate slightly from the Na-normalized silicate and basaltic end-members (Figs. 6c & d), which we tentatively attribute to the influence of weathering solutes from carbonates in sedimentary lithologies (Andjić et al., 2018), hydrothermal mineral assemblages, and veins (de Boer, 1979; Kuijpers, 1980). While measured ^{87}Sr/^{86}Sr ratios capture weathering solutes from silicate/basaltic end-members, we consider that they conservatively provide a Sr weathering signature from the mafic tropical margin at Nicoya. However, future work is needed to separate Sr weathering signals for carbonates versus silicates in the region.

Our results hold implications for seawater Sr isotope evolution and weathering histories in the Cenozoic when marine carbonates recorded increasing ^{87}Sr/^{86}Sr (~0.708 at 60 Ma; ~0.709 at present) (Raymo et al., 1988; Paytan et al., 2021). Seawater Sr isotopes reflect contributions from continental weathering, marine hydrothermal activity, and marine sedimentary processes (Edmond, 1992; Paytan et al., 2021). Increased seawater ^{87}Sr/^{86}Sr throughout the Cenozoic was proposed to reflect increases in weathering fluxes carrying high ^{87}Sr/^{86}Sr, such as those from the silicate continental crust (Raymo et al., 1988; Li & Elderfield, 2013; Li et al., 2021), the metamorphic core complex from the Himalayan Orogeny (Edmond, 1992), and/or mica minerals (Li et al., 2007). Recent studies propose that the uplift and weathering of the Southeast Asian Islands (SEAIs) made significant contributions to weathering fluxes in the late Cenozoic (Macdonald et al., 2019; Park et al., 2020). If we consider ^{87}Sr/^{86}Sr ratios (average ~0.7051) from this study representative of Sr weathering signatures from mafic margins in the tropics, this would suggest that weathering of fresh mafic rocks at the SEAIs would not directly contribute radiogenic ^{87}Sr/^{86}Sr fluxes (Park et al., 2020; Rugenstein et al., 2021). Subsquently, increased marine ^{87}Sr/^{86}Sr in the Cenozoic would require enhanced weathering fluxes from radiogenic lithologies (e.g., those in the Himalaya) (Edmond, 1992; Park et al., 2020) in tandem with rapid weathering of the SEAIs. However, future studies reconstructing the magnitude and ^{87}Sr/^{86}Sr ratios of Sr fluxes from the SEAIs and non-SEAI regions are necessary to better understand how the SEAIs influenced seawater Sr evolution and Earth's climate in the late Cenozoic.

6. CONCLUSIONS

We assess the relationship between rock uplift, denudation, and silicate weathering by studying 12 catchments across a tenfold uplift gradient at the tropical basaltic margin at the Nicoya Peninsula, Costa Rica. We obtain the following findings:

First, we estimated total denudation rates and silicate cation denudation rates from stream water chemistry, model-calibrated stream discharge and sediment flux (Syvitski et al., 2003), and unmixed solute sources. We find that across a tenfold gradient in uplift rates and under near-constant climate and lithology silicate weathering rates do not increase to the same extent, but rather vary by a factor of 5. In other words, uplift rates do not dictate silicate weathering rates in our study area. Despite favorable weathering conditions (i.e., a tropical climate and abundant mafic rock), silicate weathering occurs under kinetically-limited conditions on Nicoya.

Second, the relict, low-relief Cerro Azul surface modulates silicate weathering rates on Nicoya by separating the landscape into portions with different erosion rates and weathering timescales. We hypothesize that on top of the low-relief surface, silicate minerals reside for long enough timescales to have near-congruent weathering, closer to the supply-limited regime. In the steep transient landscape below the Cerro Azul surface, silicate minerals have less time to weather before being eroded, and silicate weathering occurs deeper within the kinetically-limited regime. These findings highlight the role that the structure and geomorphology of mountain belts have in regulating silicate weathering, suggesting that broad plateaus codeveloped with orogenic belts (e.g., the Himalayan-Tibetan system) could further enhance weathering.

Finally, this study also provides insights into the temperature-dependence and Sr signatures of basalt weathering in tropical settings. Nicoya Peninsula basalts weather at the highest mean annual temperatures (27-30°C) observed among global inactive basalt fields and demonstrate a relationship between mean annual temperature and weathering rate, supporting basalt weathering as an important feedback between chemical weathering and temperature (Dessert et al., 2003; Li et al., 2016; Chen et al., 2020). Additionally, measured $^{87}Sr/^{86}Sr$ ratios provide conservative estimates of $^{87}Sr/^{86}Sr$ ratios of young (< 2 Ga), non-radiogenic Nicoya Peninsula basalts (Gaillardet et al., 1999), and suggest that only enhancing the weathering of fresh mafic rocks would not produce the observed increase in Cenozoic marine $^{87}Sr/^{86}Sr$ ratios (Park et al., 2020).

Overall, our work provides a comprehensive picture of silicate weathering in an uplifting basaltic range on the tropical Nicoya Peninsula. Our results indicate that tectonic uplift rates do not dictate silicate weathering rates in the region. Rather, we demonstrate a kinetically-limited weathering regime even under favorable weathering conditions (e.g., high denudation rates, tropical climates, and highly weatherable mafic rocks) and a key role of geomorphology. Our findings support a temperature dependence of basalt weathering and thus a feedback between weathering and temperature. We recommend future work in more targeted studies atop and below the Cerro Azul surface to better understand how low-relief surfaces influence silicate weathering. We also recommend future efforts to separate magnitudes and $^{87}Sr/^{86}Sr$ ratios between silicates and carbonates on Nicoya to enhance our understanding of geochemical weathering signals in mafic, tropical margins.

7. FIGURES & TABLES

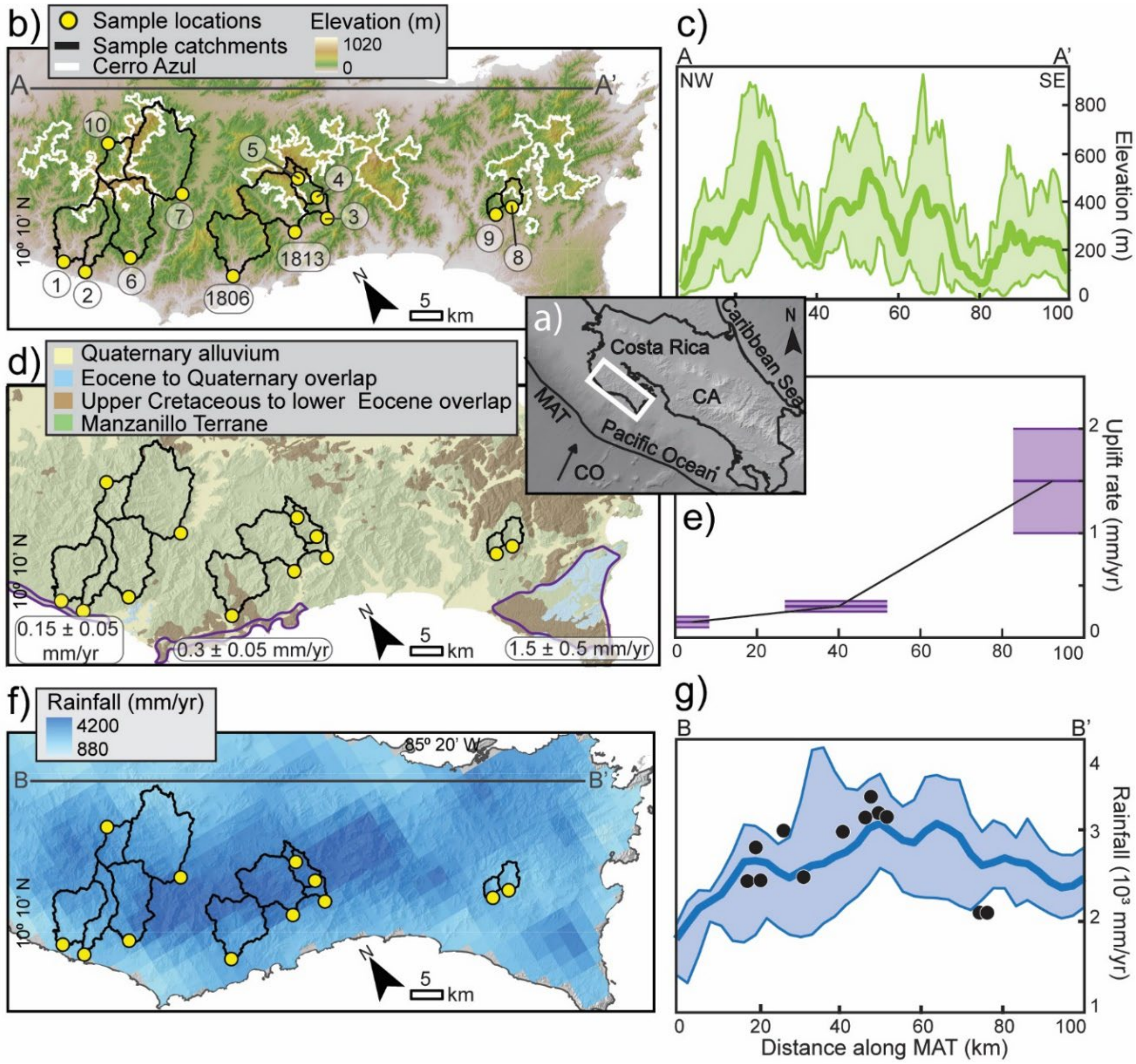

Figure 1. Map view of the study area on the Nicoya Peninsula, Costa Rican margin. (a) Tectonic setting of the Nicoya Peninsula, where the Cocos Plate (CO) subducts beneath the Caribbean Plate (CA) along the Middle America Trench (MAT), as shown by the black convergence vector. The white box outlines the study area displayed in panels, b, d, and f. Spatial data from General Bathymetric Chart of the Oceans (GEBCO) (2024). (b) 10-m resolution elevation map (Insituto Geografico Nacional Costa Rica, 2019) with sample locations, catchments, labels (Table 1), and mapped boundaries of the Cerro Azul geomorphic surface. A-A' transect delineates elevation swath profile in panel c. (c) NW to SE striking 20 km-wide elevation swath, measured along strike of the MAT. Thick solid line: mean elevations; thin solid lines: minimum and maximum elevations. (d) Geologic map simplified from Andjić et al. (2018) with sample locations and catchments. Purple outlines delineate approximate locations of Pleistocene to Holocene marine terraces with associated uplift rates (LaFromboise, 2012) displayed in panel e. (e) Uplift rates from Pleistocene to Holocene marine terraces (LaFromboise, 2012) plotted along-strike of the MAT. Central horizontal line is average uplift rate and shaded purple area is uncertainty. Black tie lines connect average uplift rates along-strike. (f) Mean annual rainfall (mm/yr) from a 4-km raster of TRMM hydrological data (Bookhagen & Burbank, 2010) with sample locations and catchments. B-B' transect delineates rainfall swath profile in panel g. (g) Corresponding 15 km-wide swath of mean annual rainfall (mm/yr) along-strike of the MAT. Thick solid line: mean rainfall; thin solid lines: minimum and maximum rainfall; black points: catchment-averaged, mean annual rainfall (Table 2).

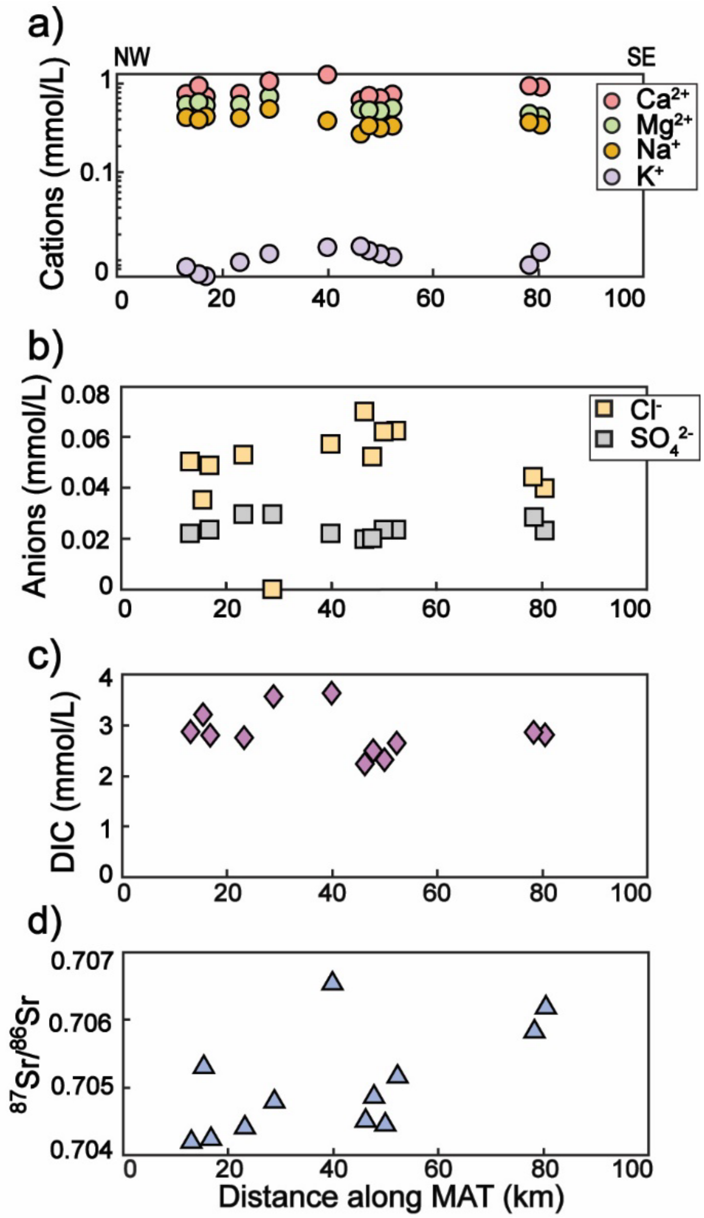

Figure 2. Along-strike variations of the concentrations (mmol/L) of (a) major cations, (b) major anions, (c) dissolved inorganic carbon (DIC), and (d) $^{87}Sr/^{86}Sr$ isotopic data (Table 1). Data are plotted from NW to SE along-strike of the Middle America Trench (Fig. 1a). Analytical uncertainties are smaller than symbols.

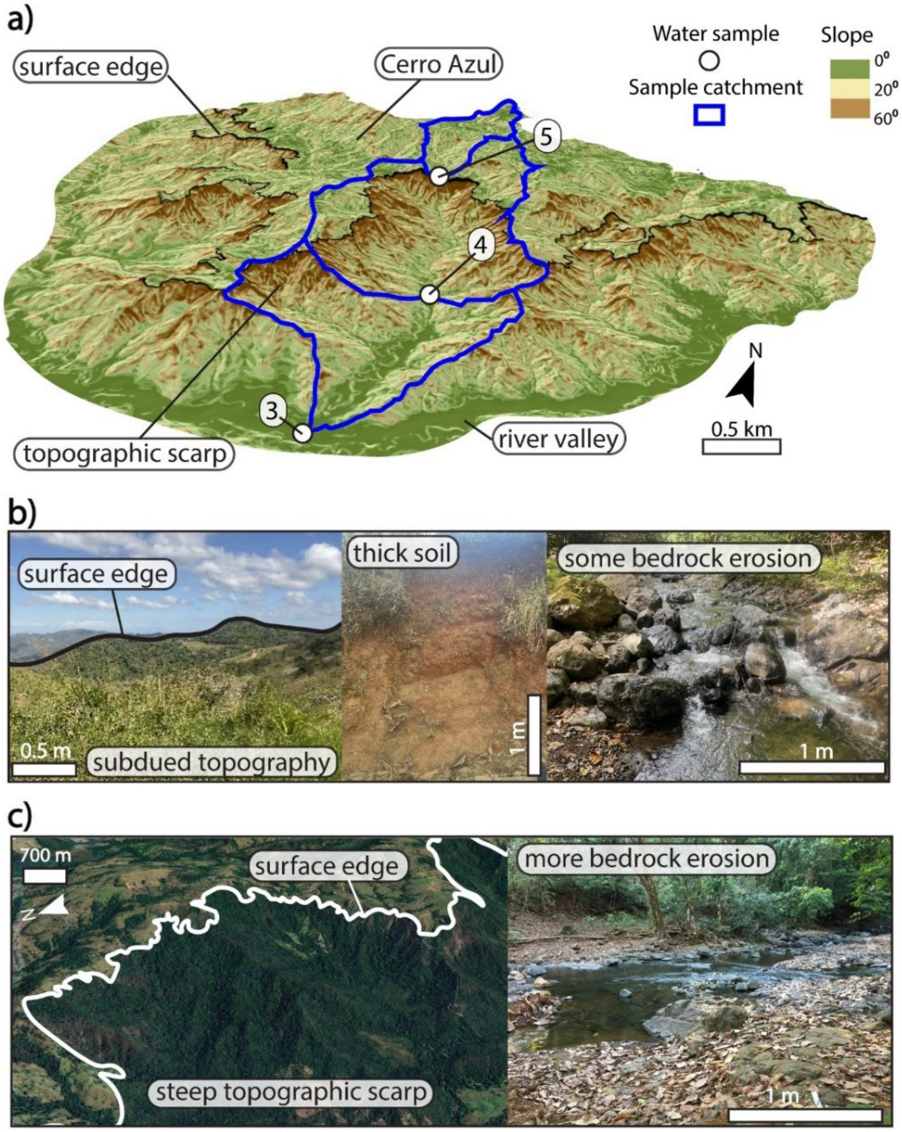

Figure 3. Views of 3 nested catchments (Samples 3-5) across a geomorphic gradient established by the Cerro Azul surface. (a) 3D view of Cerro Azul surface and associated main features on slope map derived from 10-m DEM (Insituto Geografico Nacional Costa Rica, 2019), with locations and catchments of Samples 3-5 draped on top. Vertical exaggeration 1.5 x. (b) Field photos of geomorphic characteristics on top of the Cerro Azul that are representative of conditions in the catchment for Sample 5, with subdued topography, meters-thick soils, and local bedrock streams. (c) Observations of geomorphic characteristics representative of catchments for Samples 3 and 4, where the Cerro Azul surfaces' steep topographic scarps and transiently adjusting bedrock streams produce a more dominant kinetically-limited signal. Left panel: Google Earth imagery, Right panel: field photo.

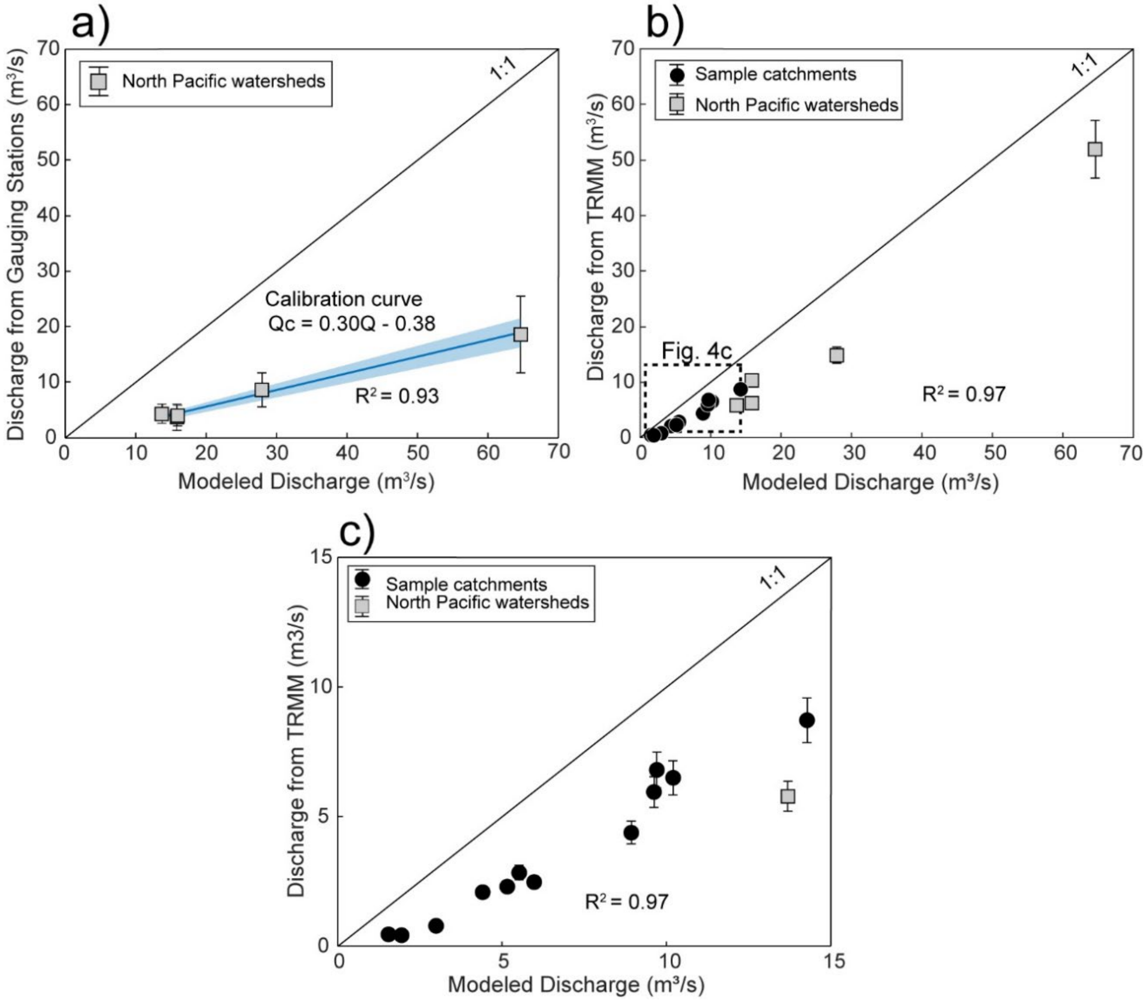

Figure 4. Calibration of global models for predicting stream discharge. (a) 1:1 plot with calibration curve constructed by weighted linear regression between numerically-modeled stream discharge (Q; Table 2; Eq. 1) (Syvitski et al., 2003) and gauged mean annual stream discharge for 5 watersheds from Costa Rica's North Pacific climate zone (Q_g; Table S2) (National Climatic Data Center, NESDIS, NOAA, U.S. Department of Commerce, 2018). Solid blue line: best-fit between data ($R^2 = 0.93$; Eq. 7; Sec. 4.3.); shaded blue region: uncertainty of fitted slope; error bars on points: $\pm 1\sigma$. (b) 1:1 plot between model-predicted stream discharge (Q; Table 2; Eq. 1) and TRMM-based (Bookhagen & Burbank, 2010) estimates of mean annual stream discharge for sampled Nicoya catchments and gauged North Pacific watersheds ($R^2 = 0.97$; Q_t; Tables 2 & S2; Eq. 2). Error bars: maximum uncertainty (± 10%) of mean annual rainfall (mm/yr) from TRMM data. (Bookhagen & Burbank, 2010). (c) Zoomed-in view of sampled catchments from (b).

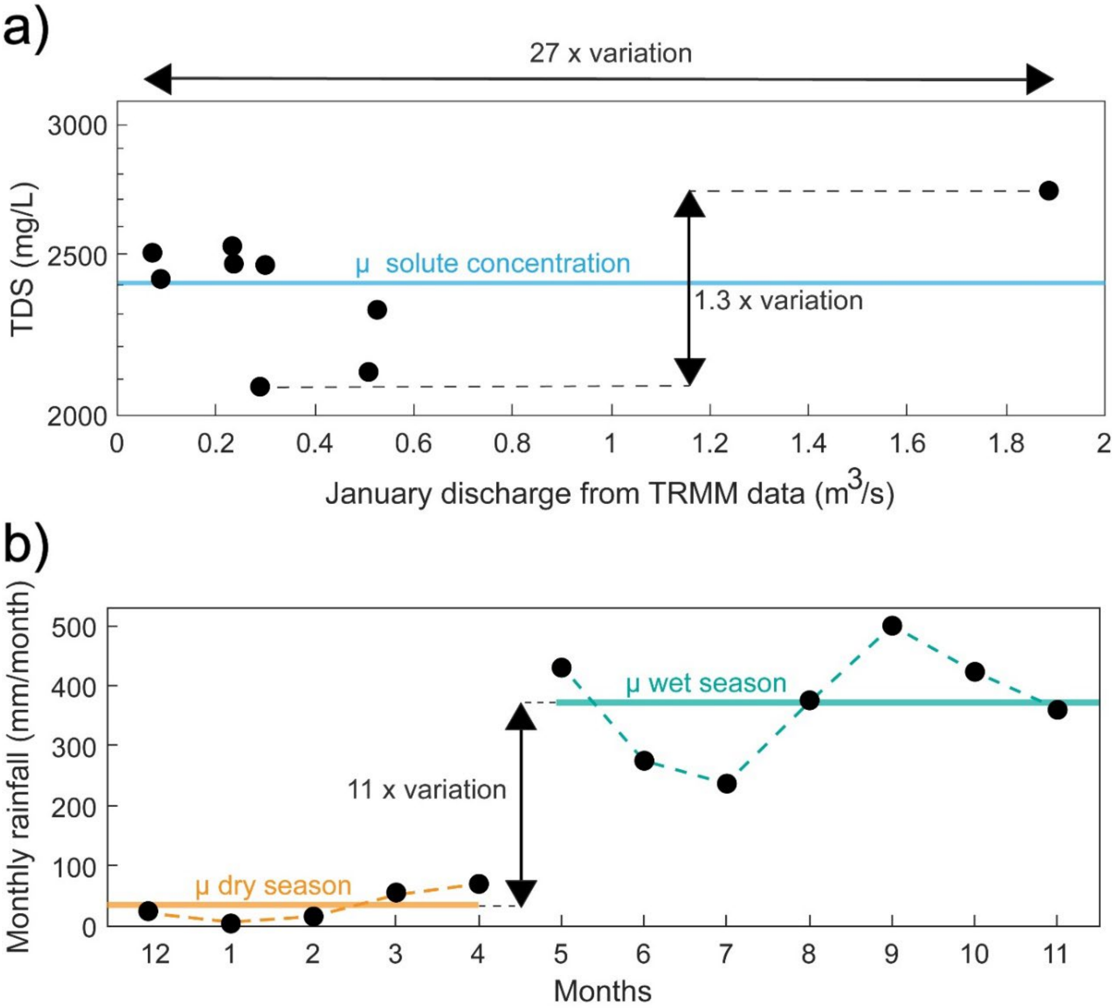

Figure 5. Variations of solute concentrations and hydrological conditions. (a) Concentration-discharge plot of TRMM-based (Bookhagen & Burbank, 2010) mean January stream discharge and January 2022 TDS concentrations from sampled catchments (Table 1). Solid blue line: mean concentration of TDS across sampled catchments (3 catchments with zero rainfall in January excluded from plot). Horizontal black arrows demonstrate 27-fold variation in January 2022 discharge across sampled catchments. Vertical arrows demonstrate variation by factor of 1.3 in TDS concentrations; dashed horizontal lines tie arrows to respective minimum and maximum TDS concentrations. (b) Mean monthly rainfall on the Nicoya Peninsula, separated into months of the dry (Dec-Apr) and wet (May-Nov) seasons denoted by dashed golden and teal lines, respectively. Solid golden and teal lines indicate mean monthly rainfall during dry and wet seasons, respectively. Vertical black arrows show 11-fold variation between mean monthly rainfall of dry and wet seasons; dashed horizontal lines tie arrows to mean monthly rainfall of dry and wet seasons.

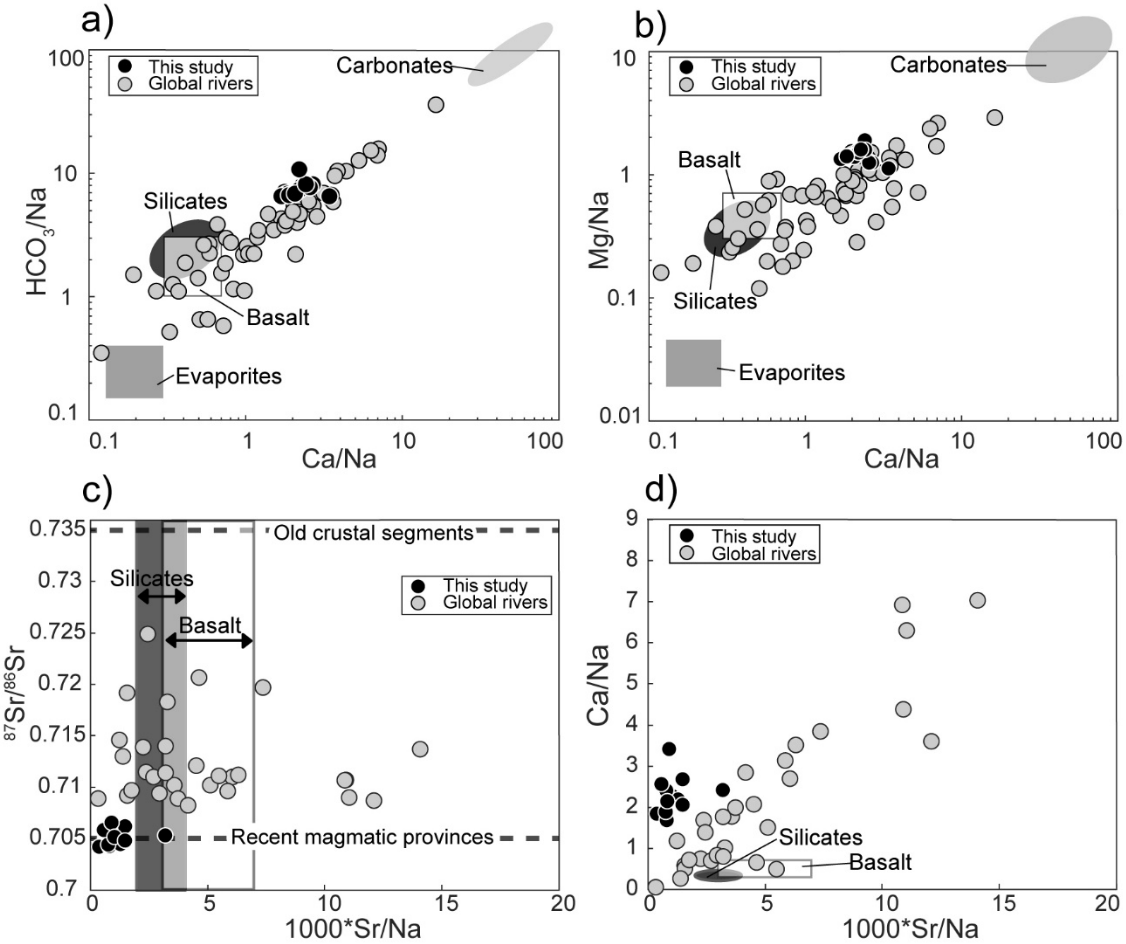

Figure 6. End-member mixing plots of Na-normalized molar ratios of data from this study (a) Ca/Na versus HCO_3/Na, (b) Ca/Na versus Mg/Na, (c) 1000*Sr/Na versus $^{87}Sr/^{86}Sr$, and (d) Sr/Na versus Ca/Na. Data are plotted with end-member Na-normalized molar ratios for evaporites, carbonates, silicates, and basalt (Gaillardet et al., 1999) and a global dataset of 60 large rivers (Gaillardet et al., 1999). In (c), $^{87}Sr/^{86}Sr$ ratios from this study are also compared with $^{87}Sr/^{86}Sr$ ratios from recent (< 2 Ga) magmatic provinces and old (2 Ga) crustal segments (Gaillardet et al., 1999).

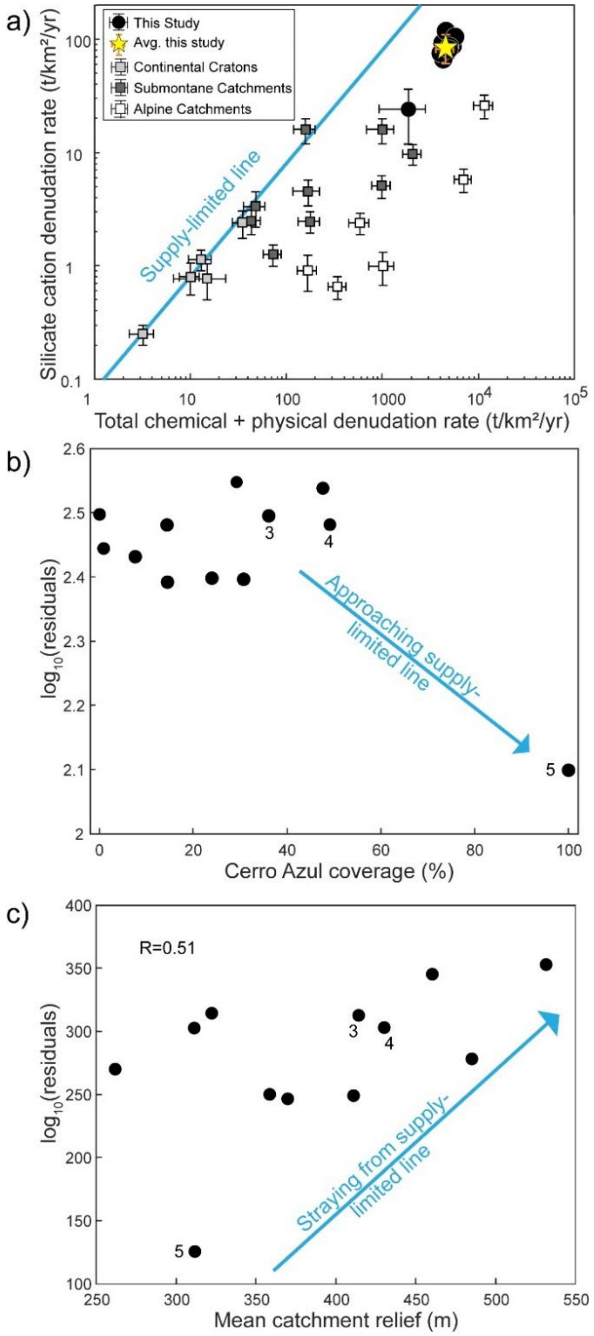

Figure 7. Relationships between silicate weathering rates, total denudation rates, and geomorphic conditions of catchments. (a) Total denudation rates (chemical + physical) versus silicate cation denudation rates of catchments from this study in the context of a global dataset (West et al., 2005). Yellow star: average of catchments from this study; solid blue line: supply-limited boundary; error bars on points: ± 1σ. (b) Percentage of catchment area covered by the Cerro Azul surface versus log$_{10}$(residuals) with residuals calculated as the distance between silicate cation denudation rates and the supply-limited line. (c) Moderate positive correlation (R = 0.51) between mean catchment relief and log$_{10}$(residuals). Samples 3-5 are nested catchments (Fig. 3). In sample catchment 5, low relief on top of the Cerro Azul surface drives weathering to occur closer to the supply-limited regime (Figs 3a & b), whereas in sample catchments 3 and 4, higher relief in the topographic scarps and transient landscape below the Cerro Azul surface drives weathering farther away from supply-limited regime (Figs. 3a & c).

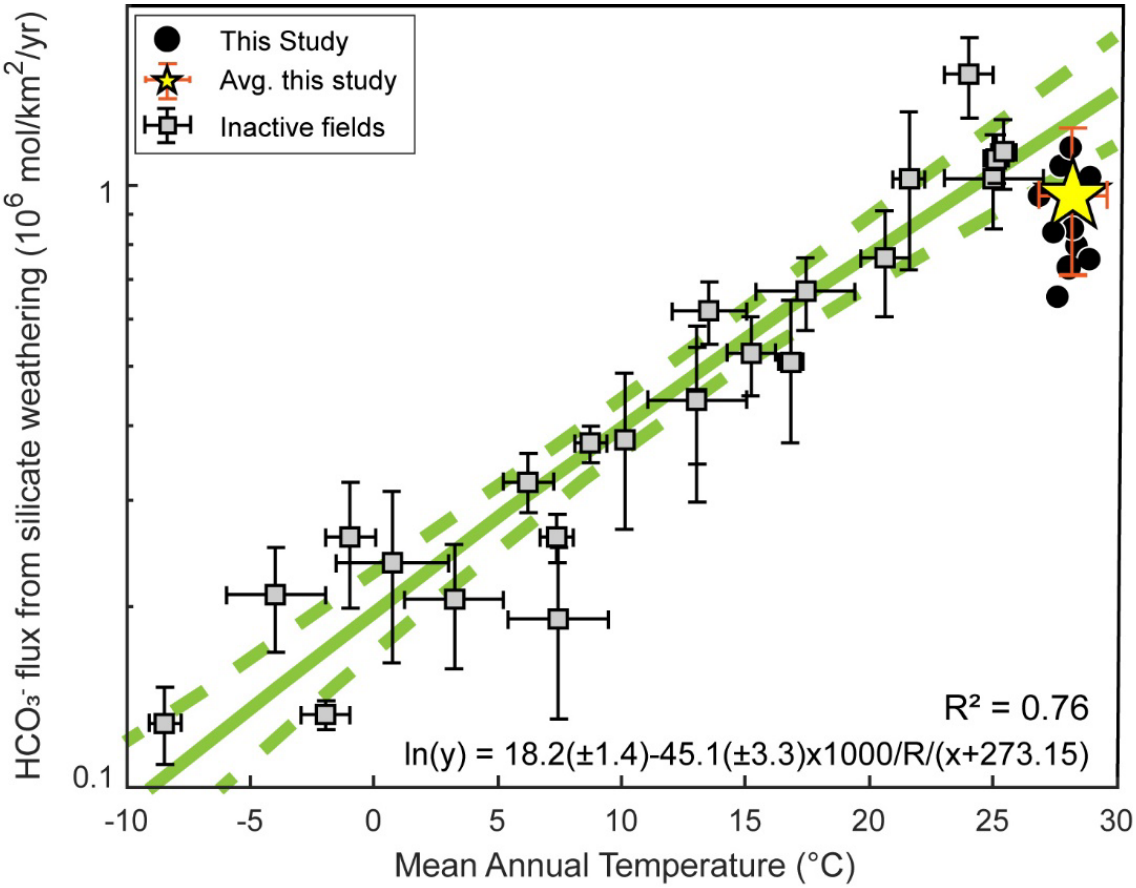

Figure 8. Correlation between mean annual temperature and weathering-induced bicarbonate flux from basalt for global dataset of inactive basalt fields (Chen et al., 2020) and data and catchment area-weighted average from this study. Solid green line shows best fit of correlation for global dataset; dashed green lines show 95% confidence intervals (Chen et al., 2020). Best-fit equation and corresponding R^2 value also displayed (Chen et al., 2020). Error bars on points: ± 1σ.

Ca^{2+} (μM)	**Mg^{2+} (μM)**	**Na^{+} (μM)**	**K^{+} (μM)**	**DIC (HCO_3^-) (μM)**	**Cl^- (μM)**	**SO_4^{2-}(μM)**	**Si (μM)**	**Sr^{2+} (μM)**	**$^{87}Sr/^{86}Sr$**	**TDS[e] (mg/L)**	**NICB %[f]**
774	588	419	8	2871	51	22	1086	0.26	0.704213	2530	3
724	572	429	7	2801	49	23	1073	0.16	0.704257	2469	2
763	535	335	11	2647	62	23	949	0.34	0.705175	2315	3
692	494	316	12	2319	62	23	964	0.34	0.704468	2123	5
656	516	272	15	2236	70	20	999	0.40	0.704519	2080	6
782	587	414	10	2754	53	30	1040	0.21	0.704422	2465	5
1073	722	521	12	3568	0	30	1139	0.31	0.704812	3071	6
924	429	345	12	2810	40	23	976	0.77	0.706201	2417	3
951	462	371	9	2861	44	28	1040	0.51	0.705842	2507	4
953	624	394	7	3210	35	35	944	0.21	0.705313	2697	4
1309	429	383	14	2496	57	22	852	1.26	0.706561	2418	2
739	507	337	13	3634	52	20	986	0.35	0.704875	2734	5

Sample	Latitude (°)	Longitude (°)	Lithology	pH	T[d] (°C)
1	85.70	10.08	MT[a] KEos[b]	nd[c]	26.5
2	85.67	10.07	MT	nd	26.2
3	85.38	9.96	MT	nd	28.8
4	85.38	9.97	MT	nd	24.7
5	85.39	10.00	MT	7	23.6
6	85.62	10.06	MT KEos	7	25.8
7	85.54	10.12	MT KEos	8	27.0
8	85.13	9.80	MT KEos	7	25.7
9	85.16	9.80	MT KEos	7	24.9
10	85.60	10.14	MT	7	25.7
1806	85.51	9.95	MT KEos	7	26.9
1813	85.43	9.97	MT KEos	7	27.5

Table 1: Major chemical composition and Sr isotopic data of sampled catchments on the Nicoya Peninsula. [a]MT=Manzanillo Terrane; [b]KEos= Cretaceous to lower Eocene overlap sequence; [c]nd=not determined; [d]T=water temperature; [e]TDS=total dissolved solids; [f]NICB=Normalized Inorganic Charge Balance of ionic species (Sec. 4.1.).

Sediment flux								
Mean elevation (m)	Mean latitude (°)	Lapse rate (°C/km)	Max relief (m)	$T_0{}^e$ (°C)	$Q_{s0}{}^f$ (kg/s)	$C_s{}^g$ (kg/m^3)	$Q_{sc}{}^h$ (kg/s)	Erosion rate (mm/yr)
203	10.0848	7.1485	444	27	6.7	0.75	1.7	0.32
325	10.0701	7.1482	533	28	5.4	0.91	1.3	0.42
414	9.9617	7.1465	589	28	5.0	0.90	1.1	0.43
487	9.9728	7.1466	595	29	4.2	0.94	0.88	0.45
686	9.9980	7.1471	514	30	1.7	1.1	0.089	0.20
382	10.0596	7.1481	513	28	6.8	0.67	1.8	0.27
381	10.1162	7.1490	556	28	8.8	0.61	2.4	0.23
394	9.8029	7.1439	662	28	3.6	1.2	0.63	0.56
306	9.8028	7.1439	618	28	3.0	1.6	0.31	0.51
491	10.1402	7.1494	721	29	5.0	1.0	1.1	0.46
284	9.9514	7.1463	464	27	6.8	0.71	1.8	0.30
371	9.9730	7.1466	565	28	7.0	0.73	1.8	0.30

Stream discharge					
Sample	**Area (km^2)**	**Q^a (m^3/s)**	**P^b (mm/yr)**	**Q_t^c (m^3/s)**	**Q_c^d (m^3/s)**
1	56	8.9	2448	4.4	2.3
2	32	6.0	2457	2.5	1.4
3	28	5.5	3154	2.8	1.3
4	21	4.4	3197	2.1	0.94
5	5	1.5	3147	0.46	0.079
6	68	10.2	3003	6.5	2.7
7	110	14.3	2493	8.7	3.9
8	12	3.0	2101	0.79	0.51
9	6	1.9	2102	0.42	0.20
10	26	5.1	2819	2.3	1.2
1806	63	9.6	2991	6.0	2.5
1813	64	9.7	3376	6.8	2.5

Table 2: Stream discharge and sediment flux data for sampled catchments.
[a]Q=modeled stream discharge (Syvitski et al., 2003) (Sec. 3.4.; Eq. 1); [b]P=Mean annual rainfall from TRMM data (Bookhagen & Burbank, 2010) (Sec. 3.4.; Fig. 1g); [c]Q_t=TRMM-derived stream discharge (Sec. 3.4.; Eq. 2); [d]Q_c=Model-calibrated stream discharge (Sec. 4.3.; Eq. 7); [e]T_0=Catchment-averaged mean annual temperatures (Sec. 3.5.; Eq. 5); [f]Q_{s0}=Modeled sediment flux (Syvitski et al., 2003) (Sec. 3.5.; Eq. 3); [g]C_s=Sediment concentration (Sec. 3.5.; Eq. 6); [h]Q_{sc}=Model-calibrated sediment flux (Sec. 4.4.; Eq. 8).

Sample	**TDR[a] (t/km^2/yr)**	**SCDR[b] (t/km^2/yr)**	**Bicarbonate flux (10^6 mol/km^2/yr)**	**% Cerro Azul surface**	**Mean relief (m)**
1	4602 ± 85	98 ± 6	0.96	8	262
2	5154 ± 153	110 ± 7	1.1	14	311
3	4931 ± 162	82 ± 5	0.80	36	414
4	4761 ± 212	78 ± 6	0.75	49	430
5	1872 ± 943	24 ± 12	0.23	100	312
6	4242 ± 67	93 ± 6	0.91	14	370
7	4604 ± 50	118 ± 7	1.2	24	359
8	5410 ± 429	87 ± 9	0.85	48	460
9	4312 ± 870	67 ± 14	0.65	1	485
10	5727 ± 203	105 ± 7	1.0	29	532
1806	5009 ± 84	86 ± 5	0.84	0	322
1813	4057 ± 69	75 ± 5	0.73	31	411
Mean and std	4557 ± 975	85 ± 24	0.93 ± 0.17	N/A	N/A

Table 3: Total denudation, weathering fluxes, and geomorphic characteristics of sampled catchments. [a]TDR=total denudation rate ± 1σ (Sec. 5.1.2.; Eq. 17); [b]SCDR=silicate cation denudation rate ± 1σ (Sec. 5.1.2.; Eq. 14).

8. REFERENCES

Andjić, G., Baumgartner, P. O., & Baumgartner-Mora, C. (2018). Rapid vertical motions and formation of volcanic arc gaps: Plateau collision recorded in the forearc geological evolution (Costa Rica margin). *Basin Research*, *30*(5), 863–894. https://doi.org/10.1111/bre.12284

Andjić, G., Baumgartner, P. O., & Baumgartner-Mora, C. (2019). Collision of the Caribbean Large Igneous Province with the Americas: Earliest evidence from the forearc of Costa Rica. *GSA Bulletin*, *131*(9–10), 1555–1580. https://doi.org/10.1130/B35037.1

Baumgartner, P. O., Mora, C. R., Butterlin, J., Sigal, J., Glacon, G., Azéma, J., & Bourgois, J. (1984). Sedimentación y paleogeografía del Cretacico y Cenozoico del Litoral Pacifico de Costa Rica. *Revista geológica de América Central*, *1*, 57–136.

Berner, R. A., Lasaga, A. C., & Garrels, R. M. (1983). *The carbonate-silicate geochemical cycle and its effect on atmospheric carbon dioxide over the past 100 million years*. *283*(7), 641–683. https://doi.org/10.2475/ajs.283.7.641

Bookhagen, B., & Burbank, D. W. (2010). Toward a complete Himalayan hydrological budget: Spatiotemporal distribution of snowmelt and rainfall and their impact on river discharge. *Journal of Geophysical Research: Earth Surface*, *115*(F3). https://doi.org/10.1029/2009JF001426

Brantley, S. L., Shaughnessy, A., Lebedeva, M. I., & Balashov, V. N. (2023). How temperature-dependent silicate weathering acts as Earth's geological thermostat. *Science*. https://doi.org/10.1126/science.add2922

Bufe, A., Cook, K. L., Galy, A., Wittmann, H., & Hovius, N. (2022). The effect of lithology on the relationship between denudation rate and chemical weathering pathways –

evidence from the eastern Tibetan Plateau. *Earth Surface Dynamics*, *10*(3), 513–530. https://doi.org/10.5194/esurf-10-513-2022

Bufe, A., Rugenstein, J. K. C., & Hovius, N. (2024). CO2 drawdown from weathering is maximized at moderate erosion rates. *Science*, *383*(6687), 1075–1080. https://doi.org/10.1126/science.adk0957

Byrne, R. H., Mackenzie, F. T., & Duxbury, A. C. (2024). Seawater. In *Encyclopedia Britannica*. https://www.britannica.com/science/seawater

Caves Rugenstein, J. K., Ibarra, D. E., & von Blanckenburg, F. (2019). Neogene cooling driven by land surface reactivity rather than increased weathering fluxes. *Nature*, *571*(7763), 99–102. https://doi.org/10.1038/s41586-019-1332-y

Chamberlin, T. C. (1899). *An Attempt to Frame a Working Hypothesis of the Cause of Glacial Periods on an Atmospheric Basis*. *7*(6), 545–584. https://doi.org/10.1086/608449

Chen, Y., Hedding, D. W., Li, X., Greyling, A. C., & Li, G. (2020). Weathering dynamics of Large Igneous Provinces (LIPs): A case study from the Lesotho Highlands. *Earth and Planetary Science Letters*, *530*, 115871. https://doi.org/10.1016/j.epsl.2019.115871

Cole, J. J., & Prairie, Y. T. (2024). Chapter 13—The Inorganic Carbon Complex. In I. D. Jones & J. P. Smol (Eds.), *Wetzel's Limnology (Fourth Edition)* (pp. 301–323). Academic Press. https://doi.org/10.1016/B978-0-12-822701-5.00013-6

de Boer, J. (1979). The outer arc of the costa rican orogen (oceanic basement complexes of the Nicoya and Santa Elena Peninsulas). *Tectonophysics*, *56*(3), 221–259. https://doi.org/10.1016/0040-1951(79)90084-2

DeMets, C., Gordon, R. G., & Argus, D. F. (2010). Geologically current plate motions. *Geophysical Journal International*, *181*(1), 1–80. https://doi.org/10.1111/j.1365-246X.2009.04491.x

Denyer, P., Aguilar, T., & Montero P., W. (2013a). *Mapa Geológico de la Hoja Cerro Azul (3145-IV)* (Primera edición) [Map]. Editorial UCR.

Denyer, P., Aguilar, T., & Montero, W. (2013b). *Mapa Geológico de la Hoja Cerro Brujo (3046-II)* (Primera edición) [Map]. Editorial UCR.

Denyer, P., Aguilar, T., & Montero, W. (2013c). *Mapa Geológico de la Hoja Diriá (3046-I)* (Primera edición) [Map]. Editorial UCR.

Denyer, P., Aguilar, T., & Montero, W. (2013d). *Mapa Geológico de la Hoja Garza (3045-I)* (Primera edición) [Map]. Editorial UCR.

Denyer, P., Aguilar, T., & Montero P., W. (2013e). *Mapa Geológico de la Hoja Matambú (3146-III)* (Primera edición) [Map]. Editorial UCR.

Denyer, P., Aguilar, T., & Montero, W. (2013f). *Mapa Geológico de la Hoja Río Arío (3145-II)* (Primera edición) [Map]. Editorial UCR

Dessert, C., Dupré, B., François, L. M., Schott, J., Gaillardet, J., Chakrapani, G., & Bajpai, S. (2001). Erosion of Deccan Traps determined by river geochemistry: Impact on the global climate and the 87Sr/86Sr ratio of seawater. *Earth and Planetary Science Letters*, *188*(3), 459–474. https://doi.org/10.1016/S0012-821X(01)00317-X

Dessert, C., Dupré, B., Gaillardet, J., François, L. M., & Allègre, C. J. (2003). Basalt weathering laws and the impact of basalt weathering on the global carbon cycle. *Chemical Geology*, *202*(3), 257–273. https://doi.org/10.1016/j.chemgeo.2002.10.001

Dessert, C., Lajeunesse, E., Lloret, E., Clergue, C., Crispi, O., Gorge, C., & Quidelleur, X. (2015). Controls on chemical weathering on a mountainous volcanic tropical island: Guadeloupe (French West Indies). *Geochimica et Cosmochimica Acta*, *171*, 216–237. https://doi.org/10.1016/j.gca.2015.09.009

Dupré, B., Dessert, C., Oliva, P., Goddéris, Y., Viers, J., François, L., Millot, R., & Gaillardet, J. (2003). Rivers, chemical weathering and Earth's climate. *Comptes Rendus Geoscience*, *335*(16), 1141–1160. https://doi.org/10.1016/j.crte.2003.09.015

Edmond, J. M. (1992). Himalayan Tectonics, Weathering Processes, and the Strontium Isotope Record in Marine Limestones. *Science*, *258*(5088), 1594–1597. https://doi.org/10.1126/science.258.5088.1594

Erikson, C. M., Renshaw, C. E., & Magilligan, F. J. (2024). Spatial variation in drainage area—Runoff relationships and implications for bankfull geometry scaling. *Geomorphology*, *446*, 108998. https://doi.org/10.1016/j.geomorph.2023.108998

Gabet, E. J., & Mudd, S. M. (2009). A theoretical model coupling chemical weathering rates with denudation rates. *Geology*, *37*(2), 151–154. https://doi.org/10.1130/G25270A.1

Gabet, E. J., Wolff-Boenisch, D., Langner, H., Burbank, D. W., & Putkonen, J. (2010). Geomorphic and climatic controls on chemical weathering in the High Himalayas of Nepal. *Geomorphology*, *122*(1), 205–210. https://doi.org/10.1016/j.geomorph.2010.06.016

Gaillardet, J., Dupre, B., Louvat, P., & Allegre, C. J. (1999). *Global silicate weathering and CO2 consumption rates deduced from the chemistry of large rivers*. *159*, 3–30. https://doi.org/10.1016/S0009-2541(99)00031-5

Godsey, S. E., Kirchner, J. W., & Clow, D. W. (2009). Concentration–discharge relationships reflect chemostatic characteristics of US catchments. *Hydrological Processes*, *23*(13), 1844–1864. https://doi.org/10.1002/hyp.7315

Hare, P. W., & Gardner, T. W. (1985). Geomorphic indicators of vertical neotectonism along converging plate margins, Nicoya Peninsula, Costa Rica. In *Tectonic Geomorphology* (Vol. 4, pp. 75–104). Allen & Unwin.

Hilton, R. G., & West, A. J. (2020). Mountains, erosion and the carbon cycle. *Nature Reviews Earth & Environment*, *1*(6), Article 6. https://doi.org/10.1038/s43017-020-0058-6

Ibarra, D. E., Caves, J. K., Moon, S., Thomas, D. L., Hartmann, J., Chamberlain, C. P., & Maher, K. (2016). Differential weathering of basaltic and granitic catchments from concentration–discharge relationships. *Geochimica et Cosmochimica Acta*, *190*, 265–293. https://doi.org/10.1016/j.gca.2016.07.006

Insituto Geografico Nacional Costa Rica. (2019). *Insituto Geografico Nacional Costa Rica*.

Jacobson, A. D., & Blum, J. D. (2003). Relationship between mechanical erosion and atmospheric CO2 consumption in the New Zealand Southern Alps. *Geology*, *31*(10), 865–868. https://doi.org/10.1130/G19662.1

Jacobson, A. D., Blum, J. D., Chamberlain, C. P., Craw, D., & Koons, P. O. (2003). Climatic and tectonic controls on chemical weathering in the New Zealand Southern Alps. *Geochimica et Cosmochimica Acta*, *67*(1), 29–46. https://doi.org/10.1016/S0016-7037(02)01053-0

Johnson, K. (2024). *Periodic table of elements in the ocean • MBARI*. MBARI. https://www.mbari.org/know-your-ocean/periodic-table-of-elements-in-the-ocean/

Kalnay, E., Kanamitsu, M., Kistler, R., & Collins, W. (1996). *The NCEP/NCAR 40-Year Reanalysis Project*. *77*, 437–471.

Kappelle, M., Lovejoy, T. E., & Gámez Lobo, R. (2016). *Costa Rican Ecosystems*. University of Chicago Press. http://ebookcentral.proquest.com/lib/ucsb-ebooks/detail.action?docID=4437689

Kirby, E., & Whipple, K. (2012). *Expression of active tectonics in erosional landscapes*. *44*, 54–75. https://doi.org/10.1016/j.jsg.2012.07.009

Kuijpers, E. P. (1980). The geologic history of the Nicoya Ophiolite Complex, Costa Rica, and its geotectonic significance. *Tectonophysics*, *68*(3), 233–255. https://doi.org/10.1016/0040-1951(80)90178-X

LaFromboise, E. J. (2012). *Neotectonism of the Nicoya Peninsula, Costa RIca: Geomorphology and Earthquake Relocations Along the Nicoya Seismic Gap* [Masters of Science in Geology, California State University, Northridge]. http://localhost/files/x346d782c

Li, G., Chen, J., Ji, J., Liu, L., Yang, J., & Sheng, X. (2007). Global cooling forced increase in marine strontium isotopic ratios: Importance of mica weathering and a kinetic approach. *Earth and Planetary Science Letters*, *254*(3), 303–312. https://doi.org/10.1016/j.epsl.2006.11.045

Li, G., & Elderfield, H. (2013). *Evolution of carbon cycle over the past 100 million years*. *103*, 11–25. http://dx.doi.org/10.1016/j.gca.2012.10.014

Li, G., Hartmann, J., & Derry, L. A. (2016). Temperature dependence of basalt weathering. *Earth and Planetary Science Letters*, *443*, 59–69. http://dx.doi.org/10.1016/j.epsl.2016.03.015

Li, L., Robinson, L. F., Li, G. K., Hedding, D. W., Xian, F., Xu, Z., Li, L., Ouyang, S., Li, T., & Li, G. (2024). Multi-isotopic constraints on the impacts of landslide on weathering and erosion in an active mountain range. *Earth and Planetary Science Letters*, *626*, 118527. https://doi.org/10.1016/j.epsl.2023.118527

Li, S., Goldstein, S. L., & Raymo, M. E. (2021). Neogene continental denudation and the beryllium conundrum. *Proceedings of the National Academy of Sciences*, *118*(42), e2026456118. https://doi.org/10.1073/pnas.2026456118

Li, S., Li, G. K., Li, W., Chen, Y., Raymo, M. E., & Chen, J. (2023). Effects of Secondary Carbonate Precipitation and Dissolution on Changjiang (Yangtze) River Chemistry and Estimates of Silicate Weathering Rates. *Global Biogeochemical Cycles*, *37*(5), e2022GB007581. https://doi.org/10.1029/2022GB007581

Liu, H.-C., You, C.-F., Huang, K.-F., & Chung, C.-H. (2012). Precise determination of triple Sr isotopes (*δ*87Sr and *δ*88Sr) using MC-ICP-MS. *Talanta*, *88*, 338–344. https://doi.org/10.1016/j.talanta.2011.10.050

Louvat, P. (1997). *Étude géochimique de l'érosion fluviale d'îles volcaniques à l'aide des bilans d'éléments majeurs et traces* [These de doctorat, Institut de physique du globe (Paris ; 1921-....)]. https://theses.fr/1997GLOB0004

Louvat, P., & Allègre, C. J. (1997). Present denudation rates on the island of Réunion determined by river geochemistry: Basalt weathering and mass budget between chemical and mechanical erosions. *Geochimica et Cosmochimica Acta*, *61*(17), 3645–3669. https://doi.org/10.1016/S0016-7037(97)00180-4

Macdonald, F. A., Swanson-Hysell, N. L., Park, Y., Lisiecki, L., & Jagoutz, O. (2019). Arc-continent collisions in the tropics set Earth's climate state. *Science*, *364*(6436), 181–184. https://doi.org/10.1126/science.aav5300

Maher, K., & Chamberlain, C. P. (2014). Hydrologic Regulation of Chemical Weathering and the Geologic Carbon Cycle. *Science*, *343*(6178), 1502–1504. https://doi.org/10.1126/science.1250770

Martin, P. E., Macdonald, F. A., McQuarrie, N., Flowers, R. M., & Maffre, P. J. Y. (2023). The rise of New Guinea and the fall of Neogene global temperatures. *Proceedings of the National Academy of Sciences*, *120*(40), e2306492120. https://doi.org/10.1073/pnas.2306492120

Meng, X., Liu, L., Balsam, W., Li, S., He, T., Chen, J., & Ji, J. (2015). Dolomite abundance in Chinese loess deposits: A new proxy of monsoon precipitation intensity. *Geophysical Research Letters*, *42*(23), 10,391-10,398. https://doi.org/10.1002/2015GL066681

Meybeck, M. (1983). Atmospheric inputs and river transport of dissolved substances. *Dissolved Loads of Rivers and Surface Water Quantity/Quality Relationships*, *141*, 173–192.

Meybeck, M. (1987). Global chemical weathering of surficial rocks estimated from river dissolved loads. *American Journal of Science*, *287*(5), 401–428.

Moon, S., Chamberlain, C. P., & Hilley, G. E. (2014). New estimates of silicate weathering rates and their uncertainties in global rivers. *Geochimica et Cosmochimica Acta*, *134*, 257–274. https://doi.org/10.1016/j.gca.2014.02.033

Moon, S., Huh, Y., Qin, J., & van Pho, N. (2007). Chemical weathering in the Hong (Red) River basin: Rates of silicate weathering and their controlling factors. *Geochimica et Cosmochimica Acta*, *71*(6), 1411–1430. https://doi.org/10.1016/j.gca.2006.12.004

Moore, A. K., Méndez Méndez, K., Hughes, K. S., & Granger, D. E. (2024). Volcanic Arc Weathering Rates in the Humid Tropics Controlled by the Interplay Between Physical Erosion and Precipitation. *AGU Advances*, *5*(2), e2023AV001066. https://doi.org/10.1029/2023AV001066

National Climatic Data Center, NESDIS, NOAA, U.S. Department of Commerce. (2018). *GRDC station data file* (No. NCEI DSI 9682) [DOS-ASCII]. The Global Runoff Data Centre. https://portal.grdc.bafg.de/applications/public.html?publicuser=PublicUser#dataDownload/Stations

Park, Y., Maffre, P., Goddéris, Y., Macdonald, F. A., Anttila, E. S. C., & Swanson-Hysell, N. L. (2020). Emergence of the Southeast Asian islands as a driver for Neogene cooling. *Proceedings of the National Academy of Sciences*, *117*(41), 25319–25326. https://doi.org/10.1073/pnas.2011033117

Paytan, A., Griffith, E. M., Eisenhauer, A., Hain, M. P., Wallmann, K., & Ridgwell, A. (2021). A 35-million-year record of seawater stable Sr isotopes reveals a fluctuating global carbon cycle. *Science*, *371*(6536), 1346–1350. https://doi.org/10.1126/science.aaz9266

Porder, S., Johnson, Arthur. H., Xing, H. X., Brocard, G., Goldsmith, S., & Pett-Ridge, J. (2015). Linking geomorphology, weathering and cation availability in the Luquillo

Mountains of Puerto Rico. *Geoderma*, *249–250*, 100–110. https://doi.org/10.1016/j.geoderma.2015.03.002

Raymo, M. E., & Ruddiman, W. F. (1992). Tectonic forcing of late Cenozoic climate. *Nature*, *359*(6391), 117–122. https://doi.org/10.1038/359117a0

Raymo, M. E., Ruddiman, W. F., Backman, J., Clement, B. M., & Martinson, D. G. (1989). Late Pliocene variation in northern hemisphere ice sheets and North Atlantic deep water circulation. *Paleoceanography*, *4*(4), 413–446. https://doi.org/10.1029/PA004i004p00413

Raymo, M. E., Ruddiman, W. F., & Froelich, P. N. (1988). Influence of late Cenozoic mountain building on ocean geochemical cycles. *Geology*, *16*(7), 649–653. https://doi.org/10.1130/0091-7613(1988)016<0649:IOLCMB>2.3.CO;2

Rugenstein, J. K. C., Ibarra, D. E., Zhang, S., Planavsky, N. J., & von Blanckenburg, F. (2021). Isotope mass-balance constraints preclude that mafic weathering drove Neogene cooling. *Proceedings of the National Academy of Sciences*, *118*(30), e2026345118. https://doi.org/10.1073/pnas.2026345118

Rust, R. H. (1983). Chapter 7 Alfisols. In L. P. Wilding, N. E. Smeck, & G. F. Hall (Eds.), *Developments in Soil Science* (Vol. 11, pp. 253–281). Elsevier. https://doi.org/10.1016/S0166-2481(08)70618-4

Ryan, P. C., Santis, A., Vanderkloot, E., Bhatti, M., Caddle, S., Ellis, M., Grimes, A., Silverman, S., Soderstrom, E., Stone, C., Takoudes, A., Tulay, P., & Wright, S. (2024). The potential for carbon dioxide removal by enhanced rock weathering in the tropics: An evaluation of Costa Rica. *Science of The Total Environment*, 172053. https://doi.org/10.1016/j.scitotenv.2024.172053

Sundquist, E., & Visser Ackerman, K. (2014). The Geologic History of the Carbon Cycle. In *Treatise on Geochemistry* (2nd ed., Vol. 10, pp. 361–398). Elsevier. http://dx.doi.org/10.1016/B978-0-08-095975-7.00809-3

Syvitski, J. P. M., Peckham, S. D., Hilberman, R., & Mulder, T. (2003). Predicting the terrestrial flux of sediment to the global ocean: A planetary perspective. *Sedimentary Geology*, *162*(1–2), 5–24. https://doi.org/10.1016/S0037-0738(03)00232-X

Torres, M. A., Baronas, J. J., Clark, K. E., Feakins, S. J., & West, A. J. (2017). Mixing as a driver of temporal variations in river hydrochemistry: 1. Insights from conservative tracers in the Andes-Amazon transition. *Water Resources Research*, *53*(4), 3102–3119. https://doi.org/10.1002/2016WR019733

Torres, M. A., West, A. J., & Clark, K. E. (2015). Geomorphic regime modulates hydrologic control of chemical weathering in the Andes–Amazon. *Geochimica et Cosmochimica Acta*, *166*, 105–128. https://doi.org/10.1016/j.gca.2015.06.007

Walker, J. C. G., & Hays, P. B. (1981). *A Negative Feedback Mechanism for the Long-Term Stabilization of Earth's Surface Temperature*. *86*(C10), 9776–9782. https://doi.org/10.1029/JC086iC10p09776

West, A., Galy, A., & Bickle, M. (2005). Tectonic and climatic controls on silicate weathering. *Earth and Planetary Science Letters*, *235*(1–2), 211–228. https://doi.org/10.1016/j.epsl.2005.03.020

West, A. J. (2012). Thickness of the chemical weathering zone and implications for erosional and climatic drivers of weathering and for carbon-cycle feedbacks. *Geology*, *40*(9), 811–814. https://doi.org/10.1130/G33041.1

Whipple, K., DiBiase, R. A., & Crosby, B. (2013). Bedrock Rivers. *Treatise on Geomorphology*, *9*, 550–573. https://doi.org/10.1016/B978-0-12-374739-6.00254-2

Wittmann, H., Blanckenburg, F., Maurice, L., Guyot, J.-L., Filizola Jr, N., & Kubick, P. W. (2011). Sediment production and delivery in the Amazon River basin quantified by in situ produced cosmogenic nuclides and recent river loads. *Geological Society of America Bulletin*, *123*, 934–950. https://doi.org/10.1130/B30317.1

Zamanian, K., Pustovoytov, K., & Kuzyakov, Y. (2016). Pedogenic carbonates: Forms and formation processes. *Earth-Science Reviews*, *157*, 1–17. https://doi.org/10.1016/j.earscirev.2016.03.003

Zhang, F., Dellinger, M., Hilton, R. G., Yu, J., Allen, M. B., Densmore, A. L., Sun, H., & Jin, Z. (2022). Hydrological control of river and seawater lithium isotopes. *Nature Communications*, *13*(1), 3359. https://doi.org/10.1038/s41467-022-31076-y

9. APPENDIX

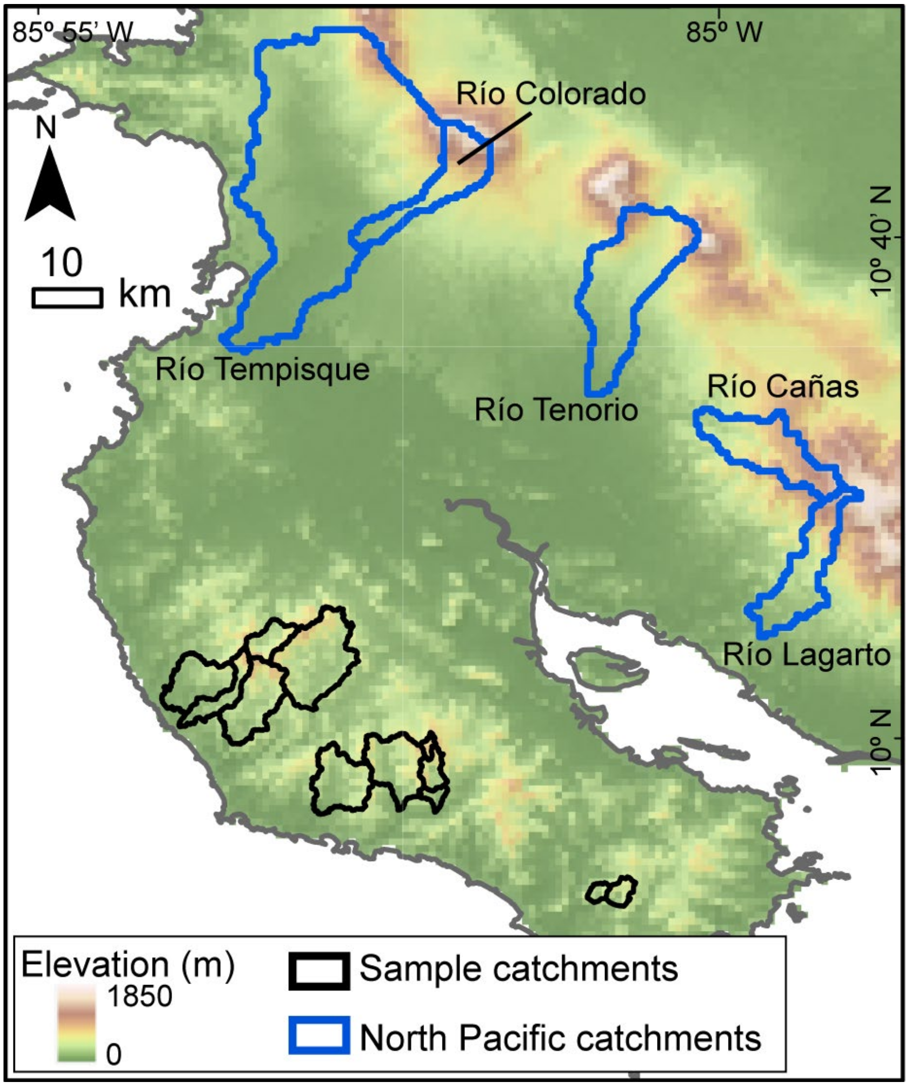

Figure S1: Map of sampled catchments on Nicoya and additional catchments from Costa Rica's North Pacific climate zone. Model estimates of stream discharge in North Pacific catchments (Syvitski et al., 2003) were compared against gauged measurements of stream discharge (National Climatic Data Center, NESDIS, NOAA, U.S. Department of Commerce, 2018) to produce the calibration curve (Eq. 7) for correction of modeled discharge in sampled catchments (Secs. 3.4. & 4.3., Fig. 4a).

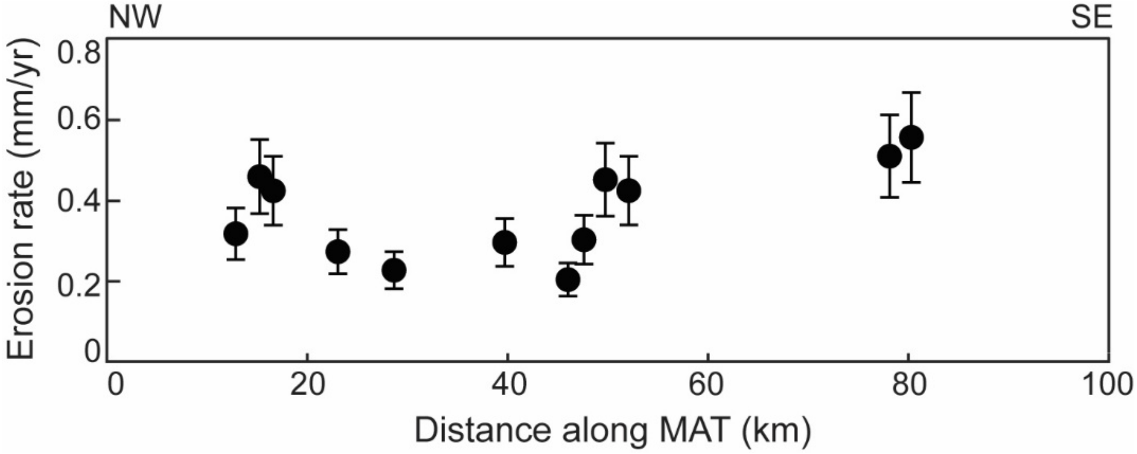

Figure S2: Short-term erosion rates from sediment yields plotted along-strike the MAT, demonstrating a general increase to the southeast, consistent with the spatial pattern and magnitude (0.15-1.5 mm/yr) of average uplift rates recorded by Pleistocene to Holocene marine terraces (Fig. 1e) (LaFromboise, 2012). Error bars indicate ± 20% of predicted values (Syvitski et al., 2003).

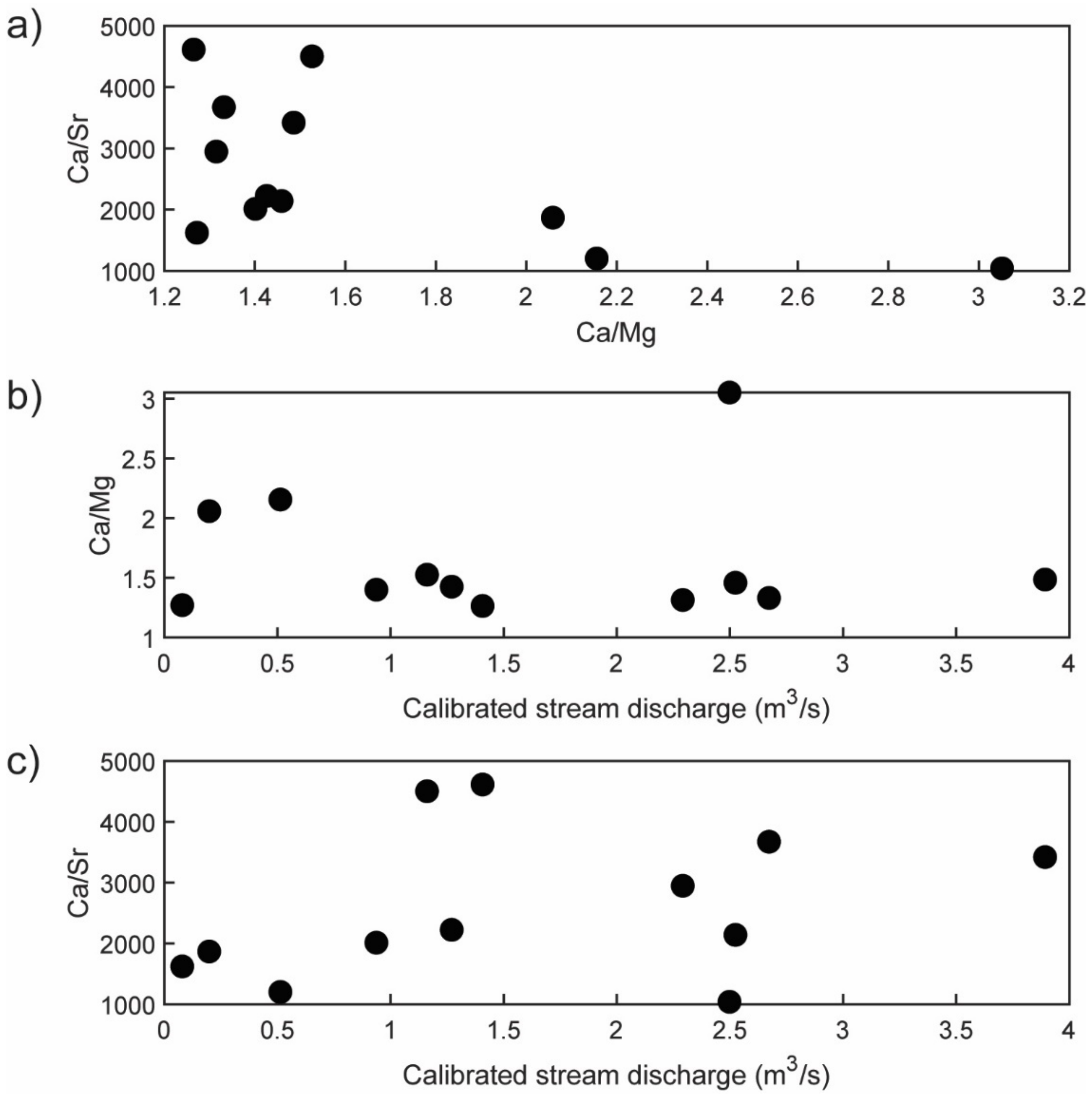

Figure S3: Relationships between (a) Ca/Mg and Ca/Sr, (b) calibrated stream discharge and Ca/Mg, and (c) calibrated stream discharge and Ca/Sr to assess potential contributions from secondary carbonate precipitation and dissolution in sampled catchments. No strongly positive correlations occur which indicates no significant inputs into riverine dissolved loads from secondary carbonates (Li et al., 2023).

<table>
<tr><th colspan="20">Stream discharge (Q) (Sec. 3.4.; Eq. 1)</th></tr>
<tr><th colspan="20">Model discharge regression coefficients for northern tropics (0-30° N) (Syvitski et al., 2003)</th></tr>
<tr><td colspan="10">α_1</td><td colspan="10">α_2</td></tr>
<tr><td colspan="10">0.53</td><td colspan="10">0.70</td></tr>
<tr><th colspan="20">Lapse rates (L(x)) (Sec. 3.5.; Eq. 4)</th></tr>
<tr><th colspan="20">Regression coefficients for lapse rate calculations (Syvitski et al., 2003)</th></tr>
<tr><td colspan="4">a_0</td><td colspan="4">a_1</td><td colspan="4">a_2</td><td colspan="4">a_3</td><td colspan="4">a_4</td></tr>
<tr><td colspan="4">2.609</td><td colspan="4">0.03</td><td colspan="4">5.464</td><td colspan="4">0.1252</td><td colspan="4">33.77</td></tr>
<tr><th colspan="20">Sediment flux (Q_{s0}) (Sec. 3.5.; Eq. 3)</th></tr>
<tr><th colspan="20">Model sediment flux regression coefficients for northern tropics (0-30° N) (Syvitski et al., 2003)</th></tr>
<tr><td colspan="5">α_3</td><td colspan="5">α4</td><td colspan="5">α5</td><td colspan="5">k</td></tr>
<tr><td colspan="5">0.31</td><td colspan="5">0.40</td><td colspan="5">0.66</td><td colspan="5">-0.1</td></tr>
</table>

Table S1: Model parameters for stream discharge, lapse rates, and sediment flux calculations.

River	Area (km^2)	Q^a (m^3/s)	P^b (mm/yr)	Q_t^{c} (m^3/s)	Q_g ^{d} (m^3/s)
Río Tempisque	955	64.6	1715	51.9	18.6
Río Colorado	128	15.8	1544	6.3	3.7
Río Tenorio	288	27.9	1628	14.9	8.6
Río Cañas	129	15.9	2531	10.3	3.9
Río Lagarto	104	13.7	1754	5.8	4.3

Table S2: Stream discharge data for North Pacific watersheds.

[a]Q=modeled stream discharge (Syvitski et al., 2003) (Sec. 3.4.; Eq. 1); [b]P=Mean annual rainfall from TRMM data (Bookhagen & Burbank, 2010) (Sec. 3.4.); [c]Qt=TRMM-derived stream discharge (Sec. 3.4.; Eq. 2); [d]Q_g=Gauged measurements of stream discharge (National Climatic Data Center, NESDIS, NOAA, U.S. Department of Commerce, 2018).

<table>
<tr><th colspan="7">Atmospheric ratios (Byrne et al., 2024; Johnson, 2024)</th></tr>
<tr><th>Ca/Na</th><th>Mg/Na</th><th>K/Na</th><th>Si/Na</th><th>HCO_3/Na</th><th>Na/Cl</th><th>SO_4/Na</th></tr>
<tr><td>0.0218</td><td>0.113</td><td>0.0227</td><td>0.029</td><td>0.005</td><td>0.8621</td><td>0.125</td></tr>
<tr><th colspan="7">Silicate end-member mixing ratios (Gaillardet et al., 1999)</th></tr>
<tr><th colspan="2">Ca/Na_{sil}</th><th colspan="3">Mg/Na_{sil}</th><th colspan="2">HCO_3/Na_{sil}</th></tr>
<tr><td colspan="2">0.35 ± 0.15</td><td colspan="3">0.24 ± 0.12</td><td colspan="2">2 ± 1</td></tr>
</table>

Table S3: Atmospheric and silicate end-member mixing ratios used in forward model (Sec. 5.1.1.)

	K^+ (µM)		HCO_3^- (µM)			Si (µM)		SO_4^{2-} (µM)	
Silicate	**Marine**	**Silicate**	**Marine**	**Silicate**	**Carbonate**	**Marine**	**Rock**	**Marine**	**Rock**
376	0.99	7.5	0.218	752	2119	1.265	1085	5.4524	16.725
387	0.96	5.7	0.211	774	2027	1.226	1072	5.2829	18.065
282	1.22	9.9	0.269	563	2084	1.559	947	6.7213	16.745
263	1.22	10.8	0.268	525	1794	1.556	962	6.7081	16.741
212	1.37	13.2	0.302	424	1812	1.754	997	7.5610	12.005
368	1.04	8.6	0.229	736	2017	1.326	1039	5.7159	24.017
521	0	12.0	0	1041	2526	0	1139	0.0000	29.539
310	0.78	11.7	0.172	620	2189	0.999	975	4.3039	18.665
332	0.87	8.1	0.192	665	2196	1.111	1039	4.7896	23.486
363	0.69	6.4	0.152	727	2483	0.882	943	3.8031	30.823
333	1.12	13.1	0.247	667	2967	1.435	850	6.1847	15.816
292	1.03	12.0	0.226	584	1912	1.309	985	5.6444	14.318

Sample	Cl^- (µM)	Ca^{2+} (µM)			Mg^{2+} (µM)			Na^+ (µM)
	Marine	**Marine**	**Silicate**	**Carbonate**	**Marine**	**Silicate**	**Carbonate**	**Marine**
1	51	0.951	132	641	4.93	90	493	43.6
2	49	0.921	135	588	4.78	93	475	42.3
3	62	1.172	99	663	6.08	68	461	53.8
4	62	1.170	92	599	6.06	63	425	53.7
5	70	1.319	74	581	6.84	51	458	60.5
6	53	0.997	129	652	5.17	88	493	45.7
7	0	0	182	891	0	125	597	0
8	40	0.751	109	815	3.89	74	350	34.4
9	44	0.835	116	834	4.33	80	378	38.3
10	35	0.663	127	825	3.44	87	534	30.4
1806	57	1.079	117	1191	5.59	80	343	49.5
1813	52	0.984	102	636	5.10	70	431	45.2

Table S4: Atmospheric, silicate and carbonate concentrations of water samples (Sec. 5.1.1).